Proton-coupled electron transfer in a pivaloyl-substituted dihydro-tetraazapentacene

Jean-François Longevial, Iryna Knysh, Shaymaa Al Shehimy, Lhoussain Khrouz, Arumugam Pandurangan, Simon Pascal, Gabriel Canard, Christophe Bucher, Denis Jacquemin, Olivier Siri

Proton-Coupled Electron Transfer in a Pivaloyl-Substituted Dihydro-Tetraazapentacene

Jean-François Longevial[a,b,*], Iryna Knysh[c], Shaymaa Al Shehimy[d], Lhoussain Khrouz[d], Arumugam Pandurangan[b], Simon Pascal[b], Gabriel Canard[b], Christophe Bucher[d,**], Denis Jacquemin[c,e,***] and Olivier Siri[b,****]

Affiliations
a *LCP-A2MC, FR 2843 Institut Jean Barriol, Université de Lorraine, ICPM, 1 Boulevard Arago, 57070 Metz Cedex 03, France*
b *Aix Marseille Univ, CNRS, CINAM, Marseille, France*
c *Nantes Université, CNRS, CEISAM UMR 6230, F-44000 Nantes, France.*
d *Univ Lyon, Ens de Lyon, CNRS UMR 5182, Laboratoire de Chimie, F69342 Lyon, France*
e *Institut Universitaire de France (IUF), Paris, FR-75005, France*

Abstract: Within the heteroacene family, azapentacenes have received much attention in organic electronic devices due to their unique physico-chemical properties. This is particularly true for the 5,14-dihydro-5,7,12,14-tetraazapentacene despite its poor solubility in organic solvents which logically hindered the study of its electrochemical behavior. Consequently, we disclose herein the synthesis and characterization of the soluble 6,13-dipivaloyl-5,14-dihydro-5,7,12,14-tetraazapentacene as well as its aromatic counterpart, the 6,13-dipivaloyl-5,7,12,14-tetraazapentacene. These compounds were used as models to fully characterize all the intermediates generated during their electrochemical processes (oxidation and reduction) with a combined approach using complementary chemical, (spectro)-electrochemical, theoretical and spectroscopic techniques. Our results demonstrate the 6,13-dipivaloyl-5,14-dihydro-5,7,12,14-tetraazapentacene ambipolar redox behavior at both cathodic and anodic regime leading to drastic color changes through proton-coupled electron transfer occuring in a totally reversible fashion.

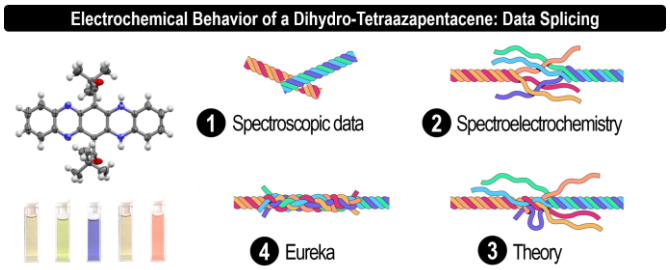

Keywords: Tetraazapentacene, redox switch, spectroelectrochemistry, radical, proton-coupled electron transfer, electrochrome.

* Corresponding author
** Corresponding author
*** Corresponding author
**** Corresponding author
E-mail addresses: jean-francois.longevial@univ-lorraine.fr (J.- F. Longevial), christophe.bucher@ens-lyon.fr (C. Bucher), denis.jacquemin@univ-nantes.fr (D. Jacquemin) and oliver.siri@univ-amu.fr (O. Siri)

1. Introduction

Within the family of polycyclic aromatic hydrocarbons (PAHs), the linearly annulated five-membered ring named pentacene has attracted much attention since its first synthesis by Clar and John in 1935 [1–4]. Due to their fascinating electronic properties as well as their ability to self-organize into dense solid state stacks, pentacene derivatives have already proved useful as hole transporters (p-type) in organic field effect transistors (OFETs) [5–8]. Unfortunately, these derivatives are also known to exhibit poor electron-transporting properties (n-type) which are the consequence of charge-losses in trap states or reactions of the reduced forms with molecular oxygen [7,9,10]. Interestingly, these drawbacks can be limited by simultaneously lowering both the HOMO and the LUMO through the incorporation of electronegative atoms such as nitrogen leading to *N*-azapentacenes [9,11–13].

N-azapentacenes are nitrogen embedded isostructural analogs of pentacenes in which the presence of nitrogen atoms offers the opportunity to manipulate and control their electronic properties, their stability, and their supramolecular arrangement in the solid state [14,15]. *N*-azapentacenes can be obtained by oxidation of the corresponding *N*-dihydro-azapentacene precursors. Among these *N*-dihydro-azapentacenes, the 5,14-dihydro-5,7,12,14-tetraazapentacene **H_2X** (Fig. 1), also known as fluorindine or 5,12-dihydroquinoxalino(2,3-*b*]phenazine, has already been used (*i*) in cosmetics [16], (*ii*) as heterogeneous catalysts [17], but more importantly as a key functional element in electronic devices including (*iii*) electrical conductors [18,19], (*iv*) organic thin-film transistors (OTFTs) [20], (*v*) organic light emitting diodes (OLEDs) [21–23], (*vi*) photovoltaic cells [24,25], and (*vii*) electrochromic devices [26]. Unfortunately, the use and characterization of **H_2X** has so far been greatly limited by its poor solubility in common organic solvents due to the combination of π-stacking interactions and H-bonds in the solid state [18,27].

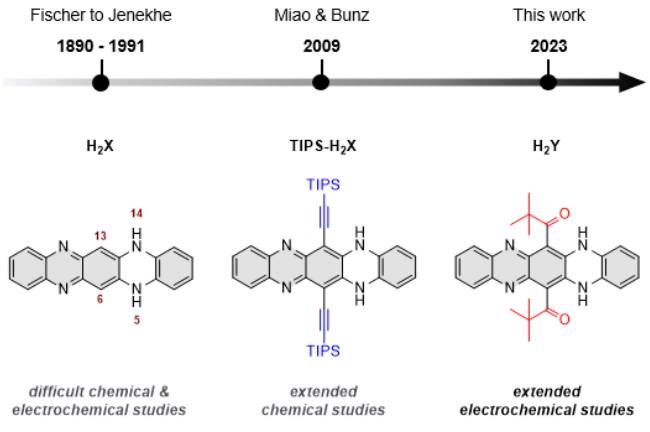

Fig. 1. Chronological appearance of 5,14-dihydro-5,7,12,14-tetraazapentacene analogs. **H_2X** is chemically and electrochemically difficult to characterize due to its very low solubility in organic solvents. **TIPS-H_2X** is soluble in organic solvents and has been chemically characterized and used in OFETs but its electrochemical behavior is still to be disclosed. **H_2Y** is an analog of **H_2X**, highly soluble in organic solvents for which we aim to disclose its full electrochemical behavior.

Additionally, **H_2X** exhibits both basic imines and potentially acidic N−H functions, meaning that its acido-basic properties are strongly dependent on its redox state [28]. In other words, **H_2X** is a perfect candidate to study intra- or intermolecular proton-coupled electron transfer (PCET) [29,30]. However, to date, the low solubility of **H_2X** and its ability to undergo PCET have greatly hampered the understanding and exploitation of its redox behavior. To our knowledge, its electrochemical characterization is limited to three articles chronologically published by Pinson (1987) [31], Jenekhe (1991) [18] and Dunsch (1995) [32]. To overcome solubility issues, Pinson worked with a substituted pyrazino[2,3-b]phenazines (tetraazatetracene) in a water/dimethylformamide (DMF) medium focusing on the cathodic domain; whereas, Jenekhe and Dunsch respectively investigated both the oxidation and reduction of the diprotonated salt **$[H_4X]^{2+}$** in DMSO and of the pristine form **H_2X** in dimethylacetamide DMMA. These studies have thus highlighted the difficulties associated to the identification of all the steps and intermediates involved in the processes coupled to electron transfer centered on azapentacene derivatives. These issues can in fact be partially overcome by increasing the solubility of **H_2X** derivatives in organic solvents through the introduction of suitable substituents. Bunz and co-workers have, for example, adapted to dihydro-tetraazapentacene an alkynylation method initially described for pentacenequinone [33], which afforded a **TIPS-H_2X** derivative [27] (Fig. 1), featuring enhanced solubilities in most organic solvents. The synthesis of this alkynylated-tetraazapentacene is now well mastered but its electrochemical characterization has so far, to the best of our knowledge, never been reported.

Given the importance of *N*-azaacene-type derivatives, particularly in electronics, and the lack of accurate reports on their physico-chemical properties, we have undertaken the synthesis of a new soluble dihydro-tetraazapentacene **H_2Y**, as well as in-depth analyses of its spectroscopic and electrochemical properties. Based on experimental data supported by Time-Dependant Density Functional Theory (TD-DFT) calculations, we have identified the mechanisms and several key intermediates involved in the coupled chemical/electrochemical processes.

2. Experimental

2.1. *Material and methods*

2.1.1. *Reagents*

Reagents were purchased from Sigma Aldrich and Alfa Aesar. Tetrahydrofuran (THF) was freshly distilled over Na^0/benzophenone. Pivaloyl chloride was distilled before use in order to remove the corresponding carboxylic acid. *n*-pentane was distilled over P_2O_5 and *n*-hexane over NaH. Column chromatography were performed using Silica gel 60 (0.040-0.063 mm) purchased from Merck. Optical properties were recorded in spectrophotometric grade solvents and when necessary in distilled THF.

2.1.2. *Analytical methods and apparatus*

Melting points (MP) were measured in open capillary tubes with a STUART SMP30 melting points apparatus and are uncorrected.

NMR spectra were recorded on a JEOL ECS400 NMR spectrometer at room temperature (25 °C or 298 K). NMR chemical shifts are given in ppm (δ) relative to Me_4Si with solvent resonances used as internal standards ($CDCl_3$: 7.26 ppm for ^1H and 77.2 for ^{13}C; DMSO-d_6: 2.50 ppm for ^1H 40.45 ppm for ^{13}C; benzene-d_6: 7.15 ppm for ^1H; toluene-d_8: 7.00 ppm for ^1H and tetrachloroethane-d_2: 6.0 ppm for ^1H). Variable temperature NMR was recorded on the above-mentioned spectrometer in benzene-d_6 or tetrachloroethane-d_2 and 8 scans accumulated spectra were recorded every 10 or 5 °C stage. The rotational barrier for compound **Y** (ΔG≠) was determined using the Eyring equation (Eq. 3) obtained and derived from the two following equations (Eq. 1 & Eq. 2):

$$k_{ex} = \frac{\pi . |\nu_a - \nu_b|}{\sqrt{2}} \quad (1)$$

$$k_{ex} = \frac{k_b . T_c}{h} . e^{\frac{-\Delta G^{\neq}}{RT}} \quad (2) \quad \leftrightarrow \quad \Delta G^{\neq} = ln\left(\frac{k_{ex} . h}{k_b . T_c}\right) . RT_c \quad (3)$$

ν_A and ν_B refers to the resonance frequency (Hz) of the desired signal in the slow exchange limit (room temperature); k_b is the Boltzmann constant (1.381 × 10^{-23} J. K^{-1}); T_c is the coalescence temperature (K); h is the Planck constant (6.62 × 10^{-34} J. s^{-1}); R is the gas constant (8.314 J. mol^{-1}. K^{-1}).

Infrared (IR) spectra were recorded on an Agilent Cary 630 FTIR equipped with an attenuated total reflectance (ATR) sampling.

High-resolution Mass Spectrometry (HRMS) analyses were performed on a QStar Elite (Applied Biosystems SCIEX) or a SYNAPT G2 HDMS (Waters) spectrometers by the "Spectropole" of the Aix-Marseille University. These two instruments were equipped with an ESI source.

UV-Vis-NIR electronic absorption spectra were recorded on a JASCO-NIR V670 spectrophotometer at room temperature with a 300 nm/min scan rate and in quartz cuvette.

Steady-state fluorescence spectra were measured using a Horiba-Jobin Yvon Fluorolog-3 spectrofluorometer. Fluorescence quantum yields Φ were measured in diluted solutions with an optical density lower than 0.1 using the following equation (eq. 4) where A is the absorbance at the excitation wavelength (λ), n the refractive index and D the integrated intensity. r and x stand for reference and sample. The fluorescence quantum yields were measured relative to rhodamine B in MeOH (Φ = 0.70) and cresyl violet in MeOH (Φ = 0.57). Excitation of reference and sample compounds was performed at the same wavelength (530 nm for **H_2Y** and 560 nm for **Y**) with 1 and 5 nm slits for **H_2Y** and **Y**, respectively.

$$\frac{\Phi_x}{\Phi_r} = \left(\frac{A_r(\lambda)}{A_x(\lambda)}\right)\left(\frac{n_x^2}{n_r^2}\right)\left(\frac{D_x}{D_r}\right) \quad (4)$$

Theoretical calculations have been performed using DFT and TD-DFT. All calculations were performed with Gaussian16.A03 [34]. Given that the considered dyes do not involve long-range charge-transfer (CT), we have chosen the M06 [35] hybrid exchange-correlation functional for all calculations. For absorption (emission) the ground (excited) state geometries were optimized with the 6-311G(d) atomic basis set, and analytical Hessian calculations have been systematically performed at the same level to ensure that the obtained structures are true minima of the potential energy surfaces. The one-photon transition energies and oscillator strengths were determined with TD-DFT using the 6-311+G(2d,p) atomic basis set and the same functional. During all calculations, environmental effects were accounted for using the Polarizable Continuum Model (PCM) selecting, as in the experiment, THF or DMF as a solvent. In the TD-DFT calculation the linear-response (LR) [36] approach was used, applying the equilibrium (non-equilibrium) limit for the optimization (transition energy) calculations. The excited states are represented by using electron density difference (EDD) plots, in which the total electronic density of the ground state is subtracted from the one of the considered excited state. These plots use a contour threshold of 0.001 au, and the blue (red) lobes represent regions losing (gaining) densities upon photon absorption, *i.e.*, donor (acceptor) moieties. Charge-transfer (CT) parameters were computed using Le Bahers' approach [37]. NICS(0) [38] values have been computed with B3LYP/6-311+G(d,p) in DMF. The vibrationally resolved spectrum were determined with the FCClasses 3.01 (v3-0.1-0177-g4b1514a) program [39,40]. We used the time-dependent formulation used either the FC approximation of the FC-HT approach (for the states with low oscillator strength, *i.e.,* the S_1 of **Y, $Y^{\cdot-}$** and **H_4Y**), and selected the so-called *Vertical Hessian* (VH) [41] vibronic model -, and used valence internal curvilinear coordinates [42]. In case of **H4Y** molecule we used the *Adiabatic Hessian* (AH) [41] model since the VH model led to unphysical adiabatic and 0-0 energies. We used a simulation temperature of 298 K. During the vibronic calculations, the vibrational contributions, energies and transition dipoles are coming from TD-DFT. The radiative and internal conversion rates have been obtained using the same methodology within the TVCF formalism [43]. For the radiative part, we used the same broadening as for the band shapes, i.e., 400 cm^{-1}, but this is known to be not important for the radiative rate [40]. For the IC part, a 10 cm^{-1} broadening Lorentzian is applied, which is a typical value in the literature [44–46] though we are well aware of the difficulty to interpret such value [45].

Electron Paramagnetic Resonance (EPR) assays were carried out at room temperature using a Bruker E500 spectrometer operating at X-band (9.3 GHz), sensitive cavity (SHQE), with 100 KHz modulation frequency. The instrument settings were as follows: microwave power; 0.26 mW; modulation amplitude; 0.5 G; Hyperfine coupling constants *a* and *g* values were obtained with simulation of experimental spectra using easyspin (Matlab toolbox). Samples were freshly prepared in a glove box and analyzed by X-Band EPR spectroscopy under an inert atmosphere.

Single crystals X-Ray Diffraction analysis (DRX). Crystals suitable for single crystal X-ray diffraction analysis were obtained by vapor diffusion of *n*-hexane into a solution of **H_2Y** in CH_2Cl_2, under an inert atmosphere for **H_2Y** ($C_{28}H_{29}N_4O_2$) and by vapour diffusion of *n*-hexane into a solution of **Y** in CH_2Cl_2, or by vapour diffusion of *n*-hexane into a saturated solution of **H_2Y** under aerobic conditions for 3 weeks for **Y** ($C_{28}H_{27}N_4O_2$). They were measured on a Rigaku Oxford Diffraction SuperNova diffractometer at room temperature at the CuKα radiation (λ = 1.54184 Å). Data collection reduction and multiscan ABSPACK correction were performed with CrysAlisPro (Rigaku Oxford Diffraction). Using Olex2 [47] the structures were solved by intrinsic phasing methods with SHELXT [48] and SHELXL [49] was used for full matrix least squares refinement. H-atoms were found experimentally but refined as riding atoms with their Uiso parameters constrained to 1.5Ueq(parent atoms) for the methyls and to 1.2Ueq(parent atom) for the other atoms. Crystal for **H_2Y** was found to be a two-domains twin with respective contributions refined as 70/30.

Electrochemistry measurements

Cyclic voltammetry (CV) and Linear Sweep Voltammetry with Rotating Disc Electrodes (LSV-RDE) were recorded using a SP300 Biologic potentiostat equipped with an 1A-48V booster. All measurements were conducted under an argon atmosphere (glove box) in a standard one-compartment, three-electrode electrochemical cell using 1,2-dichloroethane (DCE) and tetra-*n*-butylammonium hexafluorophosphate ($TBAPF_6$) as a supporting electrolyte (0.1 M). $TBAPF_6$ was prepared, purified and dried using standard procedures. 1,2-dichloroethane (DCE, anhydrous) was purchased from Sigma-Aldrich, degassed, filtered over activated alumina and stored on molecular sieves before use.

An automatic ohmic drop compensation procedure was systematically performed when using cyclic voltammetry. Vitreous carbon (Ø = 3 mm) or platinum (Ø = 2 mm) working electrodes (CH Instruments) were polished with 1 µm diamond paste before each recording. Voltamperometry with a rotating disk electrode (RDE) was carried out with a radiometer (CTV101 radiometer analytical) equipment at a rotation rate of 500 rad min^{-1} using a glassy carbon RDE tip (Ø= 3 mm). Exhaustive electrolyses were carried out in a potentiostatic regime with coulometry using a home-made divided cell and a large surface platinum working electrode as well as a carbon-based counter electrode.

Spectroelectrochemical measurements were carried out at room temperature under an argon atmosphere (glove box) using either an all-quartz immersion probe (1 mm) or a thin-layer type (0.5 mm) three-electrodes spectroelectrochemical cell with a biologic SP300 potentiostat coupled to a MCS 601/611 UV-Vis-NIR 1.7 HR Zeiss spectrophotometer. $Ag/AgNO_3$ (CH Instruments, 10^{-2} M + $TBAClO_4$ 10^{-2} M in CH_3CN) was used as a reference electrode.

2.2. *Synthesis and characterization data*

2.2.1. *Synthesis of 5,14-dihydro-5,7,12,14-tetraazapentacene **H_2X***

2,5-dihydroxyparabenzoquinone (2 g, 14 mmol, 1 equiv.), *o*-phenylenediamine (3.1g, 29 mmol, 2 equiv.) and benzoic acid (17.3 g, 142 mmol, 10 equiv.) were grinded together with a mortar. Then, the resulting powder was heated to 360 °C for 5 minutes in a round bottom flask equipped with a condenser. The reaction mixture should turn to a

deep blue color. After a 5 minutes cooling, EtOH (100-150 mL) was carefully added, and the resulting mixture was submitted to ultrasounds for 15 minutes. The resulting solid was filtered off under vacuum using a sintered glass funnel, and washed several times with EtOH, then dried under vacuum for 12 hours. The resulting solid was grinded and taken-up with 50 mL of EtOAc and submitted to ultrasound for 15 minutes. Once again, it was filtered off under vacuum with a sintered glass funnel, washed several times with EtOAc and dried overnight under vacuum. 5,14-dihydrotetraazapentacene **H_2X** was obtained as a black/blue powder with gold reflects in 60% yield (8.4 mmol, 2.4 g). The ^{1}H NMR spectrum was in accordance with the literature data [50]. **^{1}H NMR** (400 MHz, DMSO-d_6): δ = 9.71 (bs, 2H, NH), 7.67 − 7.64 (dd, 2H, $^3J_{H\text{-}H}$ = 6.3 Hz, $^4J_{H\text{-}H}$ = 2.9 Hz), 7.44 − 7.41 (dd, 2H, $^3J_{H\text{-}H}$ = 6.3 Hz, $^4J_{H\text{-}H}$ = 2.9 Hz), 6.61 − 6.59 (dd, 2H, $^3J_{H\text{-}H}$ = 5.6 Hz, $^4J_{H\text{-}H}$ = 2.3 Hz), 6.50 − 6.48 (dd, 2H, $^3J_{H\text{-}H}$ = 5.6 Hz, $^4J_{H\text{-}H}$ = 2.3 Hz), 6.33 (s, 2H).

2.2.2. *Synthesis of 6,13-dipivaloyl-5,14-dihydro-5,7,12,14-tetraazapentacene **H_2Y***

In a two-necked round bottom flask, equipped with a septum, a nitrogen inlet and a stirring bar, **H_2X** (800 mg, 2.8 mmol, 1 equiv.) was dissolved in 150 mL of distilled THF. Then, ^{n}BuLi (2.5 mL of a 2.5 M solution in hexanes, 6.3 mmol, 2.2 equiv.) was added dropwise over a period of 15 minutes at room temperature and the mixture was stirred for 2 hours. After that, trimethylacetylacylchloride (1.9 mL, 15 mmol, 7 equiv.) was added dropwise over a period of 15 minutes (the reaction mixture turned pink) and the mixture was stirred overnight at room temperature. Then, deionized H_2O (50 mL) was slowly added and the reaction mixture vigorously stirred for 15 minutes. THF was then removed under reduced pressure, and the resulting water suspension was filtered off under vacuum with a sintered glass funnel. The solid residue was dried overnight under vacuum. It was then taken up with 50 mL of dichloromethane, submitted to ultrasounds for 15 minutes and passed through a Celite pad to remove the unreacted **H_2X**. After evaporation of dichloromethane, the residue was purified by column chromatography on silica gel with CH_2Cl_2/EtOAc (99/1) as eluent to afford a deep orange/red powder after solvent evaporation. The latter powder was recrystallized from CH_2Cl_2/*n*-pentane to give **H_2Y** as an orange solid (needles) in 22% yield (0.6 mmol, 280 mg). **Rf** (SiO_2, CH_2Cl_2/EtOAc 99/1): 0.70. **MP**: 312-314 °C. **^{1}H NMR** (400 MHz, DMSO-d_6): δ = 8.66 (bs, 2H, NH), 7.64 − 7.62 (dd, 2H, $^3J_{H\text{-}H}$ = 6.5 Hz, $^4J_{H\text{-}H}$ = 3.0 Hz), 7.52 − 7.49 (dd, 2H, $^3J_{H\text{-}H}$ = 6.5 Hz, $^4J_{H\text{-}H}$ = 3.0 Hz), 6.96 − 6.93 (dd, 2H, $^3J_{H\text{-}H}$ = 5.8 Hz, $^4J_{H\text{-}H}$ = 2.3 Hz), 6.66 − 6.64 (dd, 2H, $^3J_{H\text{-}H}$ = 5.8 Hz, $^4J_{H\text{-}H}$ = 2.3 Hz), 1.26 (s, 18H) ppm. **^{13}C{^{1}H} NMR** (DMSO-d_6): δ = 211.8, 142.7, 140.2, 134.3, 128.6, 128.1, 127.1, 122.5, 114.9, 113.1, 45.6, 26.9 ppm. **FT-IR** (ATR): □ = 3336, 3271, 2960, 2867, 1662, 1756, 1575, 1478, 1450, 1360, 1271, 1064, 881, 742 cm^{-1}. **UV-vis** (CH_2Cl_2): □(□) = 505 (29 100), 536 (27 100) nm (M^{-1}. cm^{-1}). **HRMS** (ESI-TOF$^+$): calculated for [M+H$^+$]: 453.2285 ($C_{28}H_{29}N_4O_2^+$), found 453.2283 Da.

2.2.3. *Synthesis of 6,13-dipivaloyl-5,7,12,14-tetraazapentacene **Y***

H_2Y (90 mg, 0.1 mmol, 1 equiv.) was dissolved in 30 mL of degassed $CHCl_3$ then activated MnO_2 (1.40 g, 20 mmol, 100 equiv.) was added and the mixture was stirred for 48 hours at room temperature. The mixture turned from orange to a brownish/red color. MnO_2 was removed by filtration through a Celite pad and the filtrate evaporated under reduced pressure. The obtained solid was recrystallized from CH_2Cl_2/*n*-hexane to afford purple crystals of **Y** in 80% yield (0.08 mmol, 36 mg). **Rf** (SiO_2, CH_2Cl_2/EtOAc 99/1): 0.75. **MP**: 314-316 °C. **^{1}H NMR** (400 MHz, $CDCl_3$): δ = 8.13 − 8.10 (dd, 4H, $^3J_{H\text{-}H}$ = 7.0 Hz, $^4J_{H\text{-}H}$ = 3.7 Hz), 7.82 − 7.79 (dd, 4H, $^3J_{H\text{-}H}$ = 7.0 Hz, $^4J_{H\text{-}H}$ = 3.7 Hz), 1.50 (s, 6H), 1.48 (s, 12H) ppm. **^{13}C{^{1}H} NMR** ($CDCl_3$): δ = 215.5, *214.7*, 145.3, *141.1*, 141.0, 137.7, *137.6*, 132.6, *132.5*, 130.5, 45.7, *45.6*, 29.8, 27.7 ppm (*italic values correspond to the minor isomer signals*). **FT-IR** (ATR): ν = 2973, 2861, 1690, 1524, 1473, 1431, 1360, 1310, 1109, 1062, 1021, 882, 756 cm^{-1}. **UV-vis** (CH_2Cl_2): λ (ε) = 340 (4500), 358 (5200), 417s (16 800), 440 (27 500), 516 (4500), 555 (6634), 600 (6200) nm (M. cm^{-1}). **HRMS** (ESI-TOF$^+$): calculated for [M+H$^+$]: 451.2129 ($C_{28}H_{27}N_4O_2^+$), found 451.2130 Da.

2.2.4. *Synthesis of bis benzenechromium(I) 6,13-dipivaloyl-5,7,12,14-tetraazapentacene radical anion **[Y]$^{\bullet-}$***

Bis benzene chromium (7 mg, 0.033 mmol, 1 equiv.) was added to a solution of **Y** (15 mg, 0.033 mmol, 1 equiv.) in 2.5 mL of distilled THF in a Schlenk tube. After 5 minutes, *n*-hexane was added on the top of the THF solution, and the Schlenk tube was placed in refrigerator for 12 hours. Then, the small brown cristals of **[Y]$^{\bullet-}$** were collected by filtration and washed with n-hexane. **[Y]$^{\bullet-}$** (0.031 mmol, 20 mg) 95% yield. **UV-vis** (THF): λ (ε) = 452 (19 600), 768 (16 000), 856 (23 000), 1051 (1 200), 1228 (1 400), nm (M^{-1}. cm^{-1}).

3. Results and discussion

3.1. *Synthesis and characterizations*

By attempting to functionalize the *sp*^{3} nitrogen atom on positions 5 and 14 of 5,14-dihydro-5,7,12,14-tetraazapentacene (**H_2X**), we unexpectedly discovered an efficient and regioselective *C*-acylation procedure. We describe here the synthesis of the targeted 6,13-dipivaloyl-5,14-dihydrotetraazapentacene **H_2Y**, as well as its chemical oxidation into **Y**, the latter being subsequently reduced in **[Y]**□⁻ (Fig. 2).

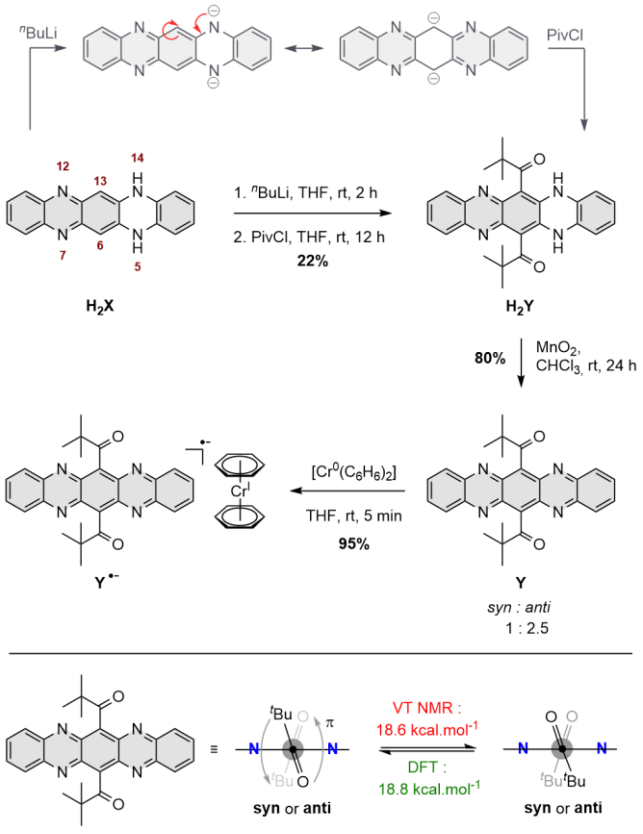

Fig. 2. Top: Synthesis of **H_2Y**, **Y** and **[Y]**□; Bottom: Rotational barrier energy for the syn/anti isomers. The DFT barrier was obtained by a relaxed PCM(DMF)-M06/6-311G(d,p) scan.

3.1.1. *Synthesis of **H_2X***

H_2X was obtained in 80% yield following our previously reported procedure, consisting in a condensation between 2 equivalents of *o*-diaminobenzene and 1 equiv. of 2,5-dihydroxy-*p*-benzoquinone in the presence of a benzoic acid excess performed at high temperature (e.g. >

300 °C) for 5 minutes [15]. The expected benzenoid form adopted by **H_2X** was confirmed by ^{1}H NMR spectroscopy measurements as previously described by Pinson (Figure S1) [32,50,51].

3.1.2. Synthesis of H_2Y, Y and [Y]$^{\bullet-}$

The functionalization of **H_2X** was achieved by adapting a methodology developed by Miao and co-workers involving use of ^{n}BuLi as a base for the deprotonation of hydrogen H_5 and H_{14} (see Fig. 2 for atom number) [52]. These authors successfully achieved the *N*-methylation of **H_2X** to afford the N_5,N_{14}-methylated benzenoid form as a major compound (55%) as well as the N_7,N_{14}-methylated quinoidal isomer (27 %) and a third benzenoid N_5,N_{14},C_6-methylated product in a non-negligible yield of 12%. The formation of the two later products was explained by the delocalization of the negative charge over the $N_{7(12)}$=C−$C_{6(13)}$=C−$N_{5(14)}$ bonds. Even though non-predominant, the *C*-functionalization − on $C_{6(13)}$ − is conceivable when considering the ambident nucleophilic character of the generated anion [53–55]. We have therefore explored the reactivity of the di-anionic form of **H_2X** with respect to other electrophiles like acyl chlorides [52]. In line with this objective, **H_2X** was deprotonated with 2 equivalents of ^{n}BuLi in THF at room temperature (Fig. 1). Addition of an excess of pivaloyl chloride (PivCl) to the mixture afforded a single product, identified as being **H_2Y**, 6,13-dipivaloyl-5,14-dihydro-5,7,12,14-dihydrotetraazapentacene isolated in 22% yield. It is worth to note that the remaining 78% of matter are composed of **H_2X** (recovered). The di-acylation of the pentacene framework was confirmed by High Resolution Mass Spectrometry (HRMS, ESI-TOF$^+$) measurements with a peak at m/z = 453.2283 Da (calculated for [M+H]$^+$: 453.2285 ($C_{28}H_{29}N_4O_2^+$)). The regioselectivity of the acylation reaction (*N vs C*) was then revealed by Infra-Red spectroscopy measurements (IR-ATR) through the observation of N−H vibrations at ν = 3271 and 3336 cm^{-1} together with the hallmark C=O stretch at − = 1662 cm^{-1}. The *C*-regioselectivity was then further demonstrated by comparison of the ^{1}H NMR spectra of **H_2Y** and **H_2X** recorded in DMSO-d_6 (Figure S3). Acylation at positions C_6 and C_{13} of **H_2X** was indeed readily revealed by the disappearance of the sharp singlet at − = 6.33 ppm attributed to H_6 and H_{13}. It was further confirmed by showing that the addition of D_2O results in the disappearance of the broad singlet at − = 8.66 ppm attributed to the N−*H*$_{5,14}$. As seen with **H_2X**, the AA'XX' ^{1}H NMR pattern observed between − = 6.50 – 7.75 ppm on the **H_2Y** spectrum in DMSO-d_6 strongly suggests the presence of a benzenoid tautomer (Figure S2). Moreover, we also found that the resonance of N−*H*$_{5,14}$ undergoes large shifts with the polarity of the solvent, going from − = 7.50 ppm in CD_2Cl_2 to − = 8.62 ppm in DMSO-d_6 (Figure S9). The formation of an enol tautomer was ruled out based on both computational studies (see below and Figure S26) and on experimental ^{13}C{^{1}H} NMR data showing that the signal corresponding to the *sp*^{2} carbonyl carbon is observed at − = 211.8 ppm.

We then checked if **H_2Y** can undergo a two-electron chemical oxidation, as described in the previous studies of Bunz and co-workers [27]. To this end, the oxidative aromatization of **H_2Y** has been attempted with organic oxidants such as DDQ (2,3-dichloro-5,6-dicyano-1,4-benzoquinone) or *p*-chloranil. These reactions led to the instantaneous formation of the targeted tetraazapentacene **Y**; but removing the oxidant from the mixture proved particularly challenging, even after several column purifications. This problem was solved by using inorganic oxidants such as Ag_2O or MnO_2, which could be removed from the reaction mixture by simple filtration. Both oxidants furnished compound **Y**, the best yield (80%) being obtained after 24 hours of stirring with activated MnO_2 in degassed $CHCl_3$. Aromatization was first confirmed by IR-ATR measurements through the disappearance of the N−H stretch signals at ν = 3271 and 3336 cm^{-1} associated with a shift of the C=O band from − = 1662 cm^{-1} (in **H_2Y**) to − = 1690 cm^{-1} (in **Y**) (Figure S12-14). The loss of two hydrogen atoms going from **H_2Y** to **Y** was then confirmed by HRMS, ESI-TOF$^+$ analysis showing a molecular peak at m/z = 451.2130 Da (calculated for [M+H]$^+$: 451.2129 ($C_{28}H_{27}N_4O_2^+$)). The ^{1}H NMR spectrum of **Y** in $CDCl_3$ also showed a highly symmetric pattern with two signals centered at − = 8.13 and 7.81 ppm, both integrating for 4 hydrogens, which are characteristic of a strong *ortho-meta* coupling. Furthermore, the spectrum also features the presence of two signals at − = 1.50 and 1.48 ppm, integrating for 18 hydrogens (total), attributed to the ^{t}Bu groups. These two signals strongly suggest the presence of two distinct populations. To confirm this hypothesis, we performed variable-temperature NMR (VT-NMR) measurements on a solution of **Y** in benzene-d_6 and tetrachloroethane-d_2. As can be seen in Figure S7-8, the two signals attributed to the ^{t}Bu substituents move closer upon heating and merge at a coalescence temperature of *ca.* 80 °C. This broad signal is then split again upon cooling back the sample to room temperature, indicating a dynamic reversible process. This phenomenon was attributed to a 180° rotation (flip) of the ^{t}Bu (or C=O) group around the mean plane containing the aromatic core of **Y** yielding a mixture of the *syn* and *anti*-isomers (Fig. 2). The activation Gibbs energy associated to this isomerization was estimated to −G− = 18.6 kcal. mol^{-1} by applying the Eyring equation. This is totally consistent with DFT calculations which led to an estimated rotational barrier of 18.8 kcal. mol^{-1}. Oxidation of **H_2Y** with MnO_2 was thus found to afford a mixture of *syn* and *anti*-isomers obtained in a 1:2.5 ratio, respectively (estimated from ^{1}H NMR data). It should be mentioned that DFT calculations carried out on both isomers suggest that they have nearly identical total energies with a theoretical difference of less than 1 kcal. mol^{-1}, *i.e.*, within DFT's error bar. The presence of these two isomers of **Y** could also be confirmed by ^{13}C{^{1}H} measurements through the observation of two sets of signals (Figure S6).

Further studies have aimed at isolating the radical anion [**Y**]$^{\bullet-}$. The later could be isolated in 95% yield from a stoichiometric mixture of [Cr^0(C_6H_6)$_2$] and **Y** in THF. The radical character of this reaction product was demonstrated by electron paramagnetic resonance (EPR) measurements. The spectrum recorded at room temperature in THF displays an intense signal at g = 2.004 indicating the presence of an unpaired electron in [**Y**]$^{\bullet-}$ (Fig. 3). The unpaired electron is also found to be delocalized over the azaacene core, as proved by the observation of hyperfine couplings with four nitrogen atoms a(^{14}N) = 1.15, 1.15, 1.63, 1.63 G, and seven hydrogen atoms a(^{1}H) = 0.57, 1.66, 1.66, 1.19, 1.19, 2.21, 2.214 G. The spin density calculated at the PCM(DMF)-U-M06/6-311+G(2d,p) for [**Y**]$^{\bullet-}$ confirms the unpaired electron delocalization within the azaacene skeleton with large contributions of the four N (N5, N7, N12 and N14) atoms as well as the two central carbon atoms (C6 and C13). These EPR data are similar to those reported by Bunz and co-workers, except that in the present case, the unpaired electron is strictly delocalized on the azaacene core and not on the substituents on positions 6 and 13, which is logical as the pivaloyl substituents are not conjugated with the azaacene rings [56,57].

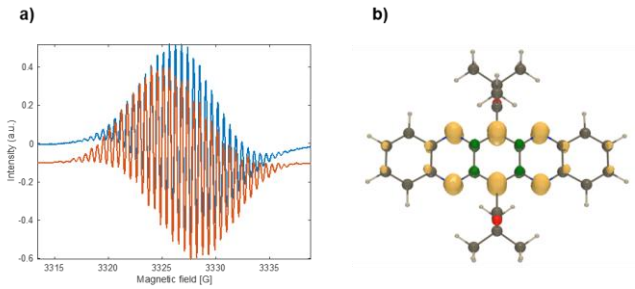

Fig. 3. a) Experimental (blue) and simulated (red) EPR spectra of [**Y**]$^{\bullet-}$ b) U-DFT spin density of [**Y**]$^{\bullet-}$ with a contour threshold of 0.005 au.

We also evaluated the stability of [**Y**]$^{\bullet-}$ in THF and found its half-life ($t_{1/2}$) to be 5 days under aerobic conditions and more than 10 days under anaerobic conditions (Figure S21).

Based on the few lifetime studies reported in the literature for similar compounds, we can conclude that [**Y**]$^{\bullet-}$ is more stable than the 6,13-

diethynyl-5,7,12,14-tetraazapentacene radical anion reported by Bunz and his collaborators [56] ($t_{1/2}$ ▯ several hours under air) but still far less stable than the tetracyano-naphtalenediimide radical anions reported by Mukhopadhyay and co-workers[58] ($t_{1/2}$ = 132 and 216 days). However, the delocalization of the spin density on these derivatives turns out to be very similar. Therefore, the substantial increase in half-life time of [**Y**]▯ may likely result from the steric protection offered by the bulky ^{t}Bu substituents [59].

3.1.3. Single crystal X-ray diffraction analysis of H_2Y and Y

We successfully obtained single crystals of both **H_2Y** and **Y**, which structures are represented in Fig. 4. The crystal structure of **H_2Y** unambiguously confirms the regioselective acylation on the central positions (6 and 13) of the tetraazapentacycle (Fig. 4a). The two ^{t}Bu groups adopts an *anti*-conformation allowing to reduce steric hindrance around that position. The O(1) and O(2) atoms are pointing toward the H(2) and H(1) atoms, forming an angle of 23.7° and 20.4° with the orthogonal mean plane passing through C(1) and C(10) atoms, respectively. Consequently, these atoms slightly interact with respective distances of 2.584 Å and 2.496 Å for C▯O(1)▯▯▯H(2)▯N(2) and C▯O(2)▯▯▯H(1)▯N(1) respectively [60]. Miao and co-workers reported the crystal structure of 6,14-dimethyl-dihydrotetrazapentacene and found a bend angle of 160° at the methylated nitrogen atom between two flat sections (the benzene ring and the diazaanthracene tricycle) [52]. This is not the case for **H_2Y** as the C▯O(1)▯▯▯H(2)▯N(2) and C▯O(2)▯▯▯H(1)▯N(1) interactions point toward opposite directions and consequently induce a rather smooth twist of the adjacent part rather than a strict bend. This specific orientation of the carbonyl groups in **H_2Y** is not present in the oxidized form **Y,** as the absence of C▯O▯▯▯H interactions makes the carbonyl groups of **Y** merged to the orthogonal mean plane passing through C(1) and C(10). As expected after aromatization, and looking at the atom deviation from the aromatic mean plane, **Y** is flatter than **H_2Y** **(**Figure S15).

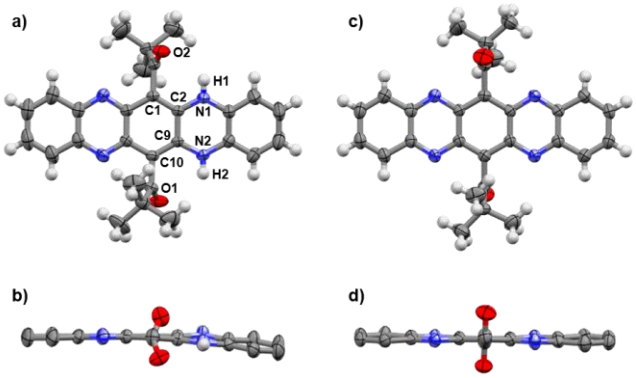

Fig. 4. Structure of **H_2Y** and **Y** determined by single crystal X-ray diffraction analyses. a) front view of **H_2Y**; b) side view of **H_2Y**; c) front view of **Y**; f) side view of **Y**.

Further analysis of the crystal lattice revealed that the packing of **H_2Y** is strongly influenced by intermolecular H-bonds (Figure S16a-b & Figure S17). Two neighboring molecules interact with an angle of 60° *via* H-bonds. An analysis of the Hirshfeld surface provides a relative proportion of the intermolecular contacts within the packing of **H_2Y** (Figure S16-17) [61–64]. The latter packing is dominated by H▯▯H interactions responsible for 60.4% of the total contacts followed by the C▯▯H contacts with 18.6% and the O▯▯H interactions 10.8% as the closest molecular contacts. The low percentage of C▯▯C contacts (3.4%) reveals that the ▯-▯ stacking interactions are almost absent. This observation can also be deduced from the curvedness (Figure S18**)** – extracted from the Hirshfeld surface – showing no flat surface patches, supporting the absence of planar stacking between molecules within the packing. This contrasts with packing of **Y**, where the curvedness analysis reveals the presence of a flat patch on its both sides and faces, revealing the presence of ▯▯▯ stacking interactions **(**Figure S19). Indeed, a planar stacking arrangement of molecules shows up as a cyan region near the center of the plot in the vicinity of (di, de) ▯ 1.7-2.1 Å, (Figure S16d) a typical range of interplanar spacing of polycyclic aromatic hydrocarbons [61]. The shortest contact between two molecules flat surface being of 3.405 Å. Consequently, **Y** adopts a "zig-zag" brick wall-type packing motif with sheets of oppositely oriented molecules (▯130°) [6,52]. As for **H_2Y**, the Hirshfeld surface analysis of **Y** (Figure S16 & S17) reveals that with 62.8%, H▯▯H contacts are predominant in the packing and belong as the shortest contacts. The relative increase of the C▯▯C (+6.2%) and C▯▯N (+3.1%) contacts in **Y** together with the decrease of C▯▯H (-12.9%) contacts is explained by the presence of ▯▯▯ stacking interactions. Despite the absence of H-bonds in the packing of **Y**, the relative compactness and molecule proximity induces an increase in the O▯▯H interactions (+2.7%) compared to **H_2Y**. Moreover, for **H_2Y**, the bond lengths are quite similar with the one reported by Miao and co-workers in 6,14-dimethyl-5,14-dihydro-5,7,12,14-terazapentacene, as for **Y**, its symmetrical bond length pattern clearly demonstrating its centrosymmetric character (Figure S20).

3.1.4. Optical and electronic properties of H_2Y, Y and [Y]$^{\bullet-}$

The UV-Vis-NIR absorption spectra collected for **H_2Y**, **Y** and [**Y**]▯ in THF are shown in Fig. 5. The spectrum of **H_2Y** exhibits two main absorption bands centered at ▯$_{max}$ = 505 nm (▯^{505} ▯ 29 000 M^{-1}. cm^{-1}) and ▯$_{max}$ = 536 nm (▯^{536} ▯ 27 000 M^{-1}. cm^{-1}). These spectroscopic signatures are in good agreement with previous data reported for 6,14-dimethyl-5,14-dihydro-5,7,12,14-tetrazapentacene and 6,13-diethynyl-5,14-dihydro-5,7,12,14-tetrazapentacene, respectively [27,52]. The absence of substantial redshift indicates the non-existent conjugation of the carbonyl groups with the main aromatic core, which is consistent with their geometry and the theoretical calculations (*vide infra*). The emission spectrum recorded for **H_2Y** exhibits one intense band at ▯$_{fl}$ = 568 nm and a vibrational component at ▯$_{fl}$ = 611 nm, with a rather large fluorescence quantum yield (▯$_F$) of 0.38 (Figure S22). The Stokes shift attains 1051 cm^{-1}. A slight positive solvatochromism of the high energy band was also observed for **H_2Y** when going to polar solvents such as MeCN, DMF or DMSO (Figure S23).

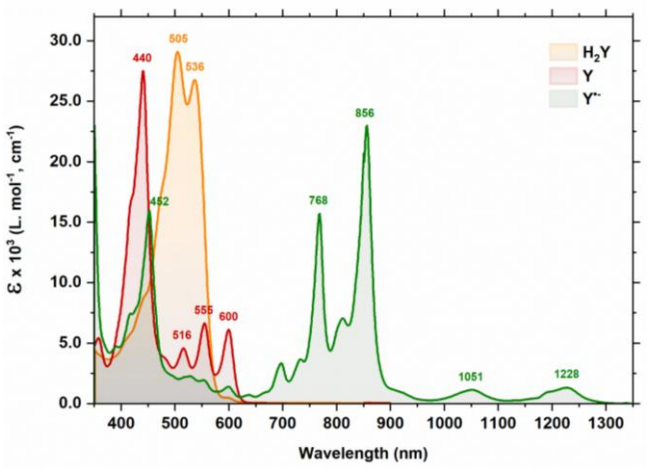

Fig. 5. UV-Vis-NIR absorption spectra of **H_2Y**, **Y** and [**Y**]▯ in THF (10^{-5} M).

Oxidation of **H_2Y** into **Y** results in a bathochromic shift (+63 nm) of the lowest energy absorption maximum from ▯$_{max}$ = 536 to ▯ $_{max}$ = 600 nm and a drastic drop of its molar extinction coefficient (~21 000 M^{-1}.cm^{-1}). The fluorescence of **Y** is also redshifted (+41 nm, Figure S22) and substantially quenched with ▯$_F$ = 0.02. The stiffness as well as the possible charge transfer from one side to another may induce a drop of

the Stokes shift of **Y** to 274 cm^{-1} [27,65]. Upon monoelectronic chemical reduction of **Y** with $[Cr^0(C_6H_6)_2]$, the near-infrared (NIR) fingerprint absorption of the open-shell radical anion $[\mathbf{Y}]^{\bullet-}$ is clearly visible (Fig. 6) [56,57]. Indeed, intense low energy band with well-defined vibrational structure appeared at λ_{max} = 768, 856 nm as well as less intense bands up to λ_{max} = 1228 nm. These data suggest that the unpaired electron is delocalized over the azapentacene aromatic core as observed by Bunz and co-workers. Unsurprisingly, the radical anion $[\mathbf{Y}]^{\bullet-}$ is non-emissive. We also estimated the aerobic and anaerobic stability of $[\mathbf{Y}]^{\bullet-}$ in THF by UV-Vis-NIR absorbance experiment (monitoring at λ = 856 nm) and confirmed the half-life ($t_{1/2}$) to be 5 days under aerobic conditions and more than twice under anaerobic conditions. The main product arising from $[\mathbf{Y}]^{\bullet-}$ decomposition is the corresponding neutral form **Y**, suggesting the stability of $[\mathbf{Y}]^{\bullet-}$ regarding disproportionation.

Behavior of H_2Y in DMF. As discussed in the previous section, the absorption spectrum of $\mathbf{H_2Y}$ in THF or in dichloromethane exhibits two intense bands at λ_{max} = 505 and 536 nm. Unexpectedly, we discovered that the absorption spectra of $\mathbf{H_2Y}$ in DMF displays additional low energy absorption bands at λ_{max} = 768 nm and 856 nm as well as less intense ones observed between 1000 and 1300 nm (Fig. 6a). Further studies have then revealed that the intensity of those additional bands increases quite significantly when decreasing the concentration of $\mathbf{H_2Y}$. This phenomenon is illustrated in Fig. 6a with selected curves showing that the low energy bands at λ_{max} = 768, 856, 1051 and 1228 nm develop upon dilution at the expense of those at λ_{max} = 505 and 536 nm attributed to $\mathbf{H_2Y}$ (with two isosbestic points at λ_{max} = 466 and 587 nm).

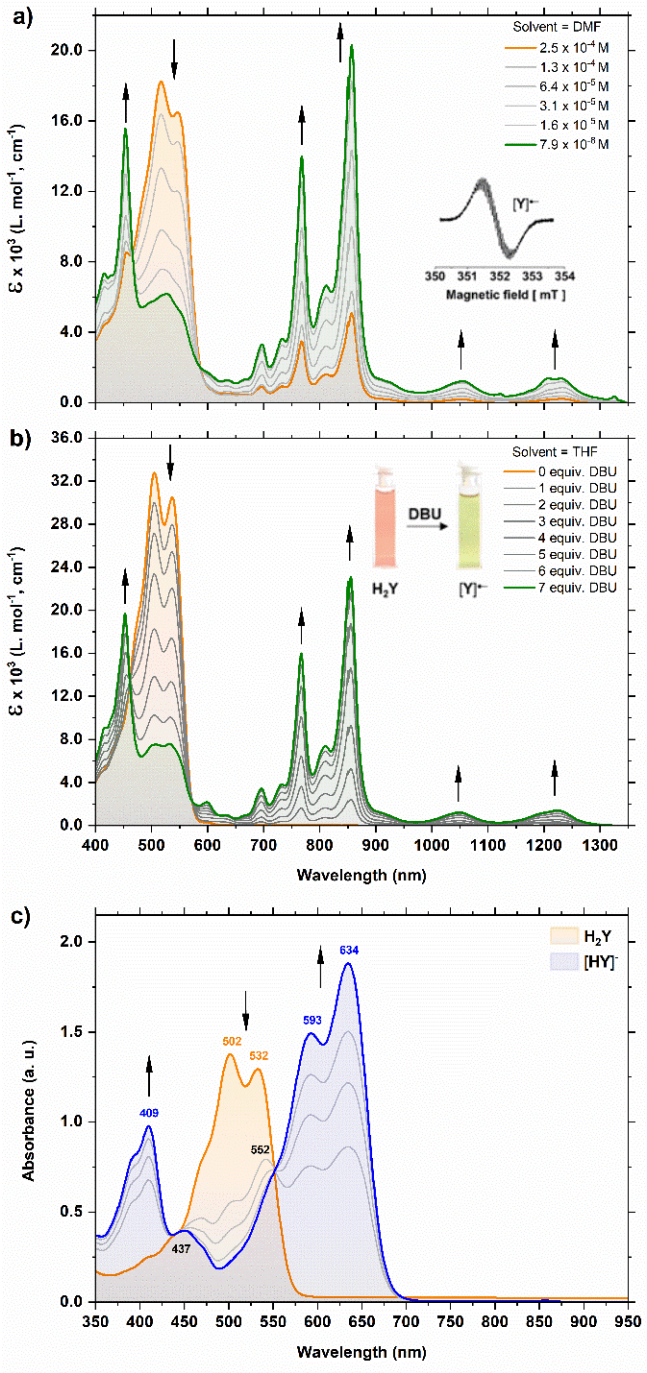

Fig. 6. a) UV-Vis-NIR absorption spectra of $\mathbf{H_2Y}$ in DMF from 2.5 x 10^{-5} M to 8.0 x 10^{-6} M, the inset is the EPR spectra of $\mathbf{H_2Y}$ into DMF: 10 mW; modulation amplitude = 0.1 G; 110 scans; [$\mathbf{H_2Y}$] = 100 µM; b) Evolution of the UV-Vis-NIR absorption spectra of $\mathbf{H_2Y}$ in THF [$\mathbf{H_2Y}$] = 1 x 10^{-5} M upon addition of DBU (1,8-diazabicyclo(5.4.0)undec-7-ene); c) anaerobic UV-Vis titration of $\mathbf{H_2Y}$ (10^{-5} M) with DBU in 1,2-dichloroethane (glove box).

These additional bands observed in DMF is in fact quite similar to the one observed by Bunz and his collaborators with radical anions of various azapentacenes [56,57]. It also matches the data recorded after chemical reduction of **Y** with $[Cr^0(C_6H_6)_2]$ (Fig. 5). These similarities thus led us to conclude that $[\mathbf{Y}]^{\bullet-}$ is actually produced *in-situ* from $\mathbf{H_2Y}$ in aerobic DMF solutions. The key role of molecular oxygen in that process was further revealed by showing that the bands attributed to $[\mathbf{Y}]^{\bullet-}$ are not observed in

oxygen-free conditions. This finding led us to study the formation kinetics of [**Y**]•⁻ by recording the absorbance over time in aerobic and anaerobic conditions at either λ_{max} = 517 nm (attributed to **H₂Y**) or λ_{max} = 856 nm (attributed to [**Y**]•⁻) in DMF (Figure S24). These measurements led to the conclusion that the disappearance of **H₂Y** in aerobic conditions is concomitant with the appearance of [**Y**]•⁻ (anaerobic conditions having no impact). EPR analyses allowed to confirm the paramagnetic character of the latter species with a signal at 352 mT featuring hyperfine couplings, suggesting a delocalization of one unpaired electron (Fig. 6a inset).

In terms of mechanism, these results prompted us to postulate that the *in-situ* formation of [**Y**]•⁻ could potentially result from the reaction of **H₂Y** with basic amine-type degradation products contained in DMF; leading to an intermediate species that quickly oxidizes in the presence of molecular O_2. This assumption was hereafter confirmed upon studying the deprotonation of **H₂Y** in both aerobic and anaerobic conditions.

Behavior of H₂Y in the presence of a base. The same absorption spectrum attributed to [**Y**]•⁻, showing peaks at λ_{max} = 768, 856, 1051 and 1230 nm, could indeed be obtained in aerobic THF by deprotonation of **H₂Y** using DBU as a base (pKa^{THF} ≈ 19) [66]. The demonstration is unambiguous since the data collected in Fig. 6b are identical (same isosbestic points and λ_{max} values) to those collected upon changing the concentration of **H₂Y** in DMF (Fig. 6a). These data are thus consistent with the conclusion that the anion radical [**Y**]•⁻ is obtained by deprotonation of **H₂Y** in the presence of O_2.

The same deprotonation experiment carried out under oxygen-free conditions (glove-box) conversely resulted in a fully different behavior, with a progressive decrease in the intensity of the signals attributed to **H₂Y** in favor of three intense absorption bands developing at λ_{max} = 409, 593 and 634 nm, which could be attributed to the monodeprotonated anion [**HY**]⁻ (Fig. 6c). This attribution is supported by both TD-DFT calculations and spectroelectrochemical data (*vide infra*). The formation of [**Y**]•⁻ in the presence of oxygen can thus be explained by an O_2-mediated oxidation of the *in-situ* generated anion [**HY**]⁻ to afford [**HY**]• which is then instantaneously deprotonated in the presence of DBU to yield [**Y**]•⁻. A similar mechanism is most likely involved in the absence of DBU when using DMF as solvent, with either solvent molecules or amine-type basic impurities acting as bases.

To the best of our knowledge, we demonstrate here for the first time that a tetraazapentacene radical anion can be either spontaneously or chemically generated from a dihydrotetraazapentacene precursor (**H₂Y**) in DMF and basic THF, respectively, highlighting the potent impact of the bulky and electron-withdrawing pivaloyl groups on the acidity of the NH.

Behavior of H₂Y in acidic media. We also studied the basicity of **H₂Y** by following the change in its UV-Vis signature during the addition of trifluoroacetic acid (TFA). As can be seen in Fig. 7, the progressive addition of TFA (from 1 to 10 molar equivalents) led to a decrease of the absorption maxima of **H₂Y** at λ_{max} = 500 and 532 nm and to the development of a new broad signal showing peaks at λ_{max} = 586 nm and 624 nm. These bands, reaching their maximum intensities after addition of 10 equivalents of TFA, have been attributed to the monoprotonated specie [**H₃Y**]⁺ based on theoretical and spectroelectrochemical data (*vide infra*).

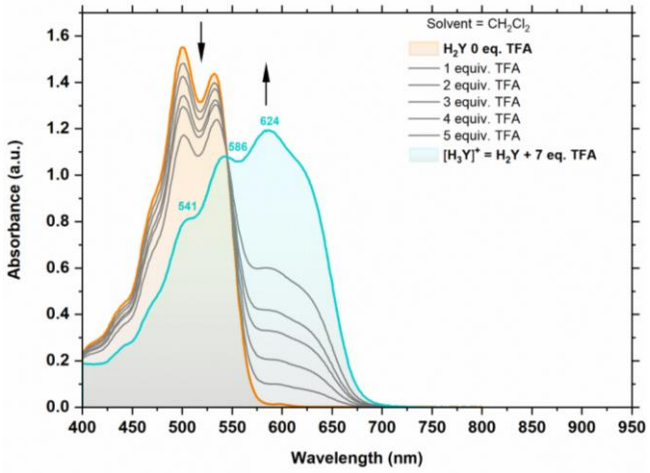

Fig. 7. Titration of **H₂Y** (10^{-5} M) in dichloromethane with increasing equivalents of trifluoroacetic acid

3.1.5. *Theoretical calculations*

To gather more information regarding the nature of the ground and excited states of the different compounds, we relied TD-DFT. First, for **H₂Y**, three tautomers (Figure S26) can be envisaged and the most stable obtained by theory actually corresponds to the one observed by single crystal X-ray diffraction analysis. An investigation of the aromaticity of **H₂Y** by the NICS approach reveals that all cycles are aromatic (NICS between −3.1 and −7.0 ppm) except the cycle bearing the two secondary amines (+6.7 ppm, Fig. 8). Vertical TD-DFT calculations in THF return a bright S_0-S_1 transition at 496 nm (f = 0.710) corresponding to the strong absorption band in the experimental spectrum (ca. 520 nm, see Fig. 5). In chemical terms, this transition mainly involves a rather delocalized yet asymmetric density reorganization (Fig. 9), with a non-trifling charge-transfer (CT) character (Fig. 9). To confirm this assignment, we performed vibrationally resolved calculations the agreement between theory and experimental band shapes is clear for both absorption and emission (Fig. 6/10 & Figure S22/S28-S30). Interestingly, such vibronic calculations also allow evaluating the emission rates considering only the radiative and internal conversion phenomena (hence neglecting other non-radiative process, *e.g.*, intersystem crossing). For **H₂Y**, such calculations deliver a fluorescence quantum yield of Φ_f = 0.42, in the very same range as the experimental value (0.38).

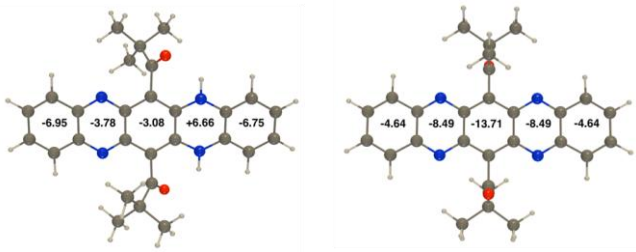

Fig. 8. NICS(0) values computed for **H₂Y** (left) and **Y** (right).

In **Y**, the central and nitrogen-bearing cycles become strongly aromatic, at the small expense of a partial decrease of aromaticity for the peripheric rings as compared to **H₂Y** (Fig. 8). Indeed, the central cycle has a NICS(0) value of −13.7 ppm. Vertical TD-DFT absorption returns a S_0-S_1 transition at 653 nm, redshifted as compared to **H₂Y**, but more importantly, showing a much lower oscillator strength (f = 0.071). This transition corresponds to the absorption band at ca. λ = 516-599 nm in the experimental domain (Fig. 5), as confirmed again by vibronic calculations (see Fig. 10 and Figure S30). This transition involves a symmetric

electronic reorganization on the whole core (Fig. 9). For **Y**, theoretical calculations performed with the same approach as for **H_2Y** return a fluorescence quantum yield of 0.04, consistent with the experimental value of 0.02.

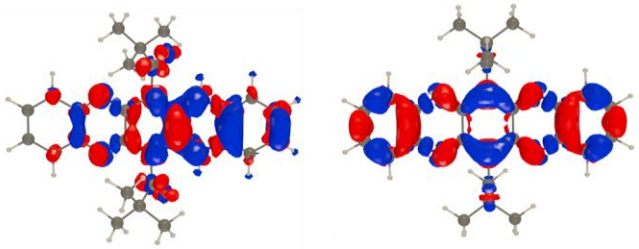

Fig. 9. EDD plots for the lowest transitions of **H_2Y** (left) and **Y** (right). The red (blue) lobes correspond to regions of increase (decrease) of density upon photoexcitation. 0.001 contour threshold.

The experimental UV-Vis absorption of [**Y**]$^{\bullet-}$ is obviously much more complex with several bands of different shapes, intensities and positions (Fig. 5). In THF, vertical TD-DFT calculations return three significantly dipole-allowed transitions at 1103 nm (f = 0.030), 713 nm (f = 0.277), and 434 nm (f = 0.511). The EDD plots for these transitions are displayed in the SI, and have the expected symmetric and delocalized topology (Figure S31). As radical species are elusive, we also performed vibronic calculations to simulate more accurately the optical spectra of [**Y**]$^{\bullet-}$ accounting for the three transitions described above. The results are shown in Fig. 10. The agreement with experiment is satisfying with two strongly redshifted and rather broad low-intensity bands above 1000 nm, coming from the S_1 excited-state, followed by much sharper peaks in the 600-800 nm domain, originating from the second excited state. Finally, a band at significantly higher energy in the 500-400 nm domain corresponds to the S_0- S_7 transition. The theoretical relative intensities are not perfect as compared to experiment, as expected for radicals. Nevertheless, the match clearly confirms that the experimental spectra displayed in Fig. 5 is the one of [**Y**]$^{\bullet-}$.

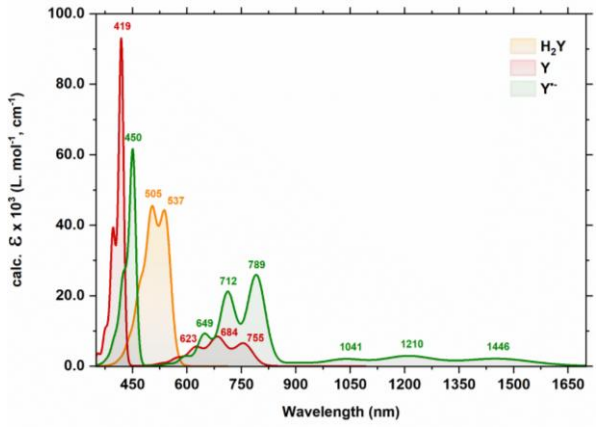

Fig. 10. Vibrationally resolved absorption spectra of **H_2Y**, **Y** and [**Y**]$^{\bullet-}$ in THF simulated using a TD approach and applying the Vertical Hessian vibronic model.

Vibronic calculations were also performed for the neutral (fully reduced form), deprotonated and protonated species, namely **H_4Y**, [**HY**]$^-$, [**H_3Y**]$^+$ and [**H_4Y**]$^{2+}$, respectively (Fig. 11). The agreement with experiment is again satisfying (e.g., see Fig. 7/10). More in details, the increasing degree of protonation of **H_2Y** induces successive redshifts, consistent with the protonation experiments A comparison between theoretical and experimental spectra hint that upon titration with an acid, the predominant specie is the monoprotonated [**H_3Y**]$^+$ and that a huge excess of acid is needed to reach the diprotonated specie [**H_4Y**]$^{2+}$ (not observed upon titration with TFA). Moreover, the simulated UV-Vis spectrum of the deprotonated specie [**HY**]$^-$ globally fits with the one displayed in Fig. 6c (intense vibronic bands at ca. 600 nm, smaller less resolved peak at ca. 400 nm) suggesting that the formation of [**Y**]$^{\bullet-}$ by deprotonation of **H_2Y** goes through the formation and successive transformation of [**HY**]$^-$.

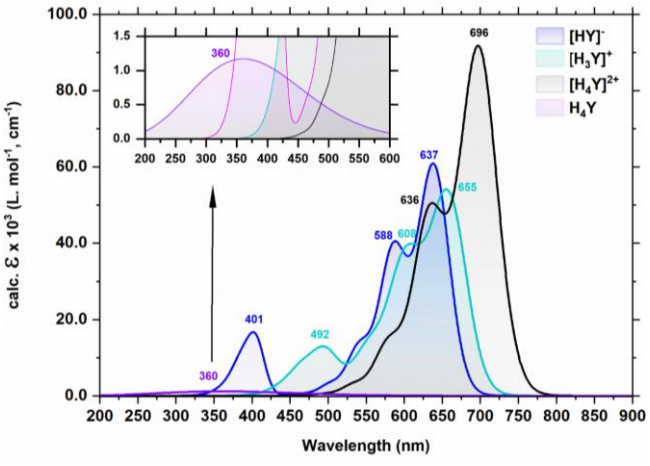

Fig. 11. Vibrationally resolved absorption spectra of **H_4Y**, [**HY**]$^-$, [**H_3Y**]$^+$ and [**H_4Y**]$^{2+}$ in THF simulated by vibrationally-resolved TD-DFT calculations.

3.1.6. Electro- and spectroelectrochemical measurements

The electrochemical properties of both **Y** and **H_2Y** were investigated in 1,2-dichloroethane (DCE) under N_2 (glove box) using a three-electrode setting involving a platinum working electrode and an $Ag/AgNO_3$ (10^{-2} M in acetonitrile) reference electrode. Selected data recorded in steady state (LSV-RDE) and transient (CV) regimes over the accessible potential window are displayed in Fig. 12.

Y was found to undergo two successive one-electron reductions centered at $E_{1/2}$ = –0.610 V and $E_{1/2}$ = –1.165 V. The number of electrons exchanged in those two redox processes was assessed from coulometry and steady state data. First insights into the stability of the reduced forms came from the fully reversible character of these two well-defined waves affording [**Y**]$^{\bullet-}$ and [**Y**]$^{2-}$, whose stability at the CV time scale (25-200 mV.s^{-1}) is consistent with a delocalization of the single electron and/or charge over the π-conjugated backbones.

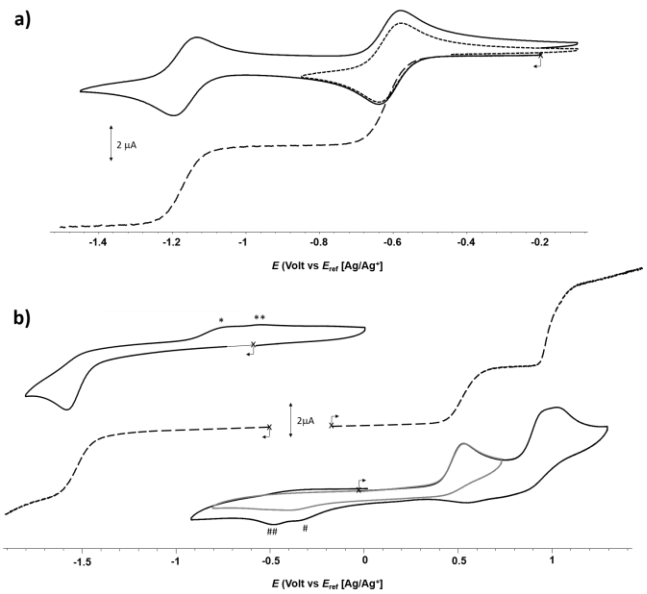

Fig. 12. Cyclic (full lines) and linear sweep (dashed curves) voltammograms recorded for a) **Y** and b) **H₂Y**; in 1,2-dicloroethane under argon in the presence of tetra-*n*-butylammonium hexafluorophosphate ($TBAPF_6$). ([C]= 0.5 mM in 0.1 M $TBAPF_6$/DCE, E (V) vs. Ag^+/Ag 10^{-2} M). CV (Pt WE Ø = 2 mm =100 $mV.s^{-1}$); LSV at RDE (GC WE Ø = 3 mm, = 5 $mV.s^{-1}$, 500 $rd.min^{-1}$).

H₂Y was found to exhibit rather different electrochemical signatures with two successive one electron oxidation waves at E_p = 0.530 V and 1.025 V and one reduction at E_p = −1.590 V. All these waves were found to retain their fully irreversible features at all accessible scan rates. The broad shape of the second oxidation wave observed at E 0.8 V and the relative value of the corresponding diffusion limited current (dashed curve) are moreover consistent with the existence of a sequence of electrochemical processes leading to the removal of more than one electrons/moles. Attribution of this irreversibility to the existence of chemical steps coupled to the oxidation and reduction processes was first supported by the observation of additional waves observed on the return scan (signals signaled by * and # in Fig. 12). In accordance with its more reduced delocalized π system and with the presence of two secondary amines, **H₂Y** was thus found to be both harder to reduce and easier to oxidize than its **Y** parent. Its reduced form [**H₂Y**] was likewise found to be far less stable than its [**Y**] counterpart generated *in-situ* by one electron reduction of **Y**. We underline that the electrochemical signature of the pivaloyl-substituted **H₂Y** shows major differences with that reported for the unsubstituted parent compound, which was found to undergo three consecutive reductions, including two reversible ones, and one oxidation in the accessible potential domain [32]. These major differences therefore bring to light the major impact of the pivaloyl electron-withdrawing substituents on both the energy and stability of the electrogenerated species produced from **H₂Y**.

The electrochemical and chemical steps involved with **Y** and **H₂Y** were further investigated by spectroelectrochemical (SEC) methods, which involved regularly recording absorption spectra over time during electrolyzes experiments carried out either at preparative or thin-layer scales.

Reduction of H₂Y. As seen in the spectra collected in Fig. 13a, the reduction of **H₂Y** in a thin-layer setup led to the gradual decrease in the intensity of the signals centered at λ_{max} = 502 and 533 nm in favor of new signals developing at $_{max}$ = 409, 593 and 635 nm, this evolution being accompanied by two well-defined isosbestic points at λ = 429 and 556 nm.

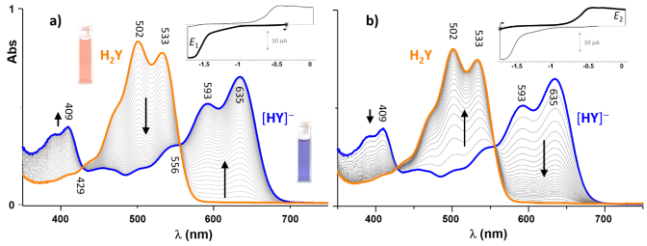

Fig. 13. UV-Vis spectra recorded over time for a solution of **H₂Y** (0.1 M $TBAPF_6$ in DCE) placed in a thin-layer spectroelectrochemical cell (0.5 mm, Pt grid) when the potential of the platinum grid was swept linearly a) from −0.35 V to E_1 = −1.7 V at 20 $mV.s^{-1}$, followed by 5 minutes of potentiostatic electrolysis at −1.7 V) and b) from −1.7 V back to E_2 = 0 V at 20 $mV.s^{-1}$, followed by 5 minutes of potentiostatic electrolysis at 0 V.

In line with the CV data discussed above demonstrating the instability of [**H₂Y**] at short timescale, EPR analyzes carried out on the bluish solution obtained after exhaustive reduction at E_{app} = −1.7 V revealed the diamagnetic character of the reaction product(s) accumulated in the cell during the forward scan (Fig. 13a). The latter species could moreover be re-oxidized upon scanning back the electrode potential to 0 V, which led to a complete regeneration of the initial sample of **H₂Y**, easily identified from the absorption bands centered at λ_{max} = 502 and 533 nm (Fig. 13b). Taken together, these CV and SEC data therefore confirm the conclusion that the electrogenerated [**H₂Y**] is readily transformed into a stable diamagnetic product, which get in turn oxidized at about 0.5 V to yield back the starting material **H₂Y** (see inset of Fig. 13b). Further insights into the nature of the chemical steps coupled to the reduction of **H₂Y** were provided upon studying its deprotonation in oxygen-free conditions using DBU as a base. As can be seen in Fig. 6c, the progressive addition of DBU to a solution of **H₂Y** in DCE +$TBAPF_6$ led to a drop in the intensity of the signals attributed to **H₂Y** in favor of three new bands, developing at $_{max}$ = 409, 593 and 635 nm with a clean isosbestic point at 552 nm, attributed to the deprotonated species [**HY**]$^-$ It should be emphasized here that this attribution is consistent with the optical spectra of [**HY**]$^-$ simulated by TD-DFT (Fig. 11) and with the assumption that the second deprotonation should be much more difficult to achieve than the first one. In addition, CV measurements carried out on an electrolytic solution of **H₂Y** obtained after addition of 10 molar equivalents of DBU also revealed that the *in-situ* generated anion [**HY**]$^-$ gets oxidized at −0.5 V (Figure S32), which is consistent with the wave observed in the backward scan of Fig. 13b. The spectroscopic and electrochemical data collected after reduction or deprotonation of **H₂Y** thus support the conclusion that the reduction of **H₂Y** at $E \leq -1.5$ V yields the anion [**HY**]$^-$ which can be reoxidized at $E \geq -0.5$ V to regenerate **H₂Y**. The mechanism shown in Fig. 14 (Eq. 1 to 5) is therefore proposed based on the experimental data collected with **H₂Y** and previous studies involving π-radicals behaving as weak Bronsted acids [28]. This mechanism is also consistent with the reversibility of the transformation and has been preferred to another possible route involving the irreversible formation of H_2 and [**HY**] from [**H₂Y**]. The first step is the one electron reduction of **H₂Y** at $E \leq -1.5$ V yielding the anion radical [**H₂Y**] which is basic enough to pull off a proton from the weak acid **H₂Y** to afford the deprotonated anion [**HY**] and the neutral radical [**H₃Y**] The latter radical species is then spontaneously reduced at the applied potential ($E \leq -1.5$ V) into the basic species [**H₃Y**], which is again capable of pulling off a proton from the remaining **H₂Y** to yield the fully reduced specie **H₄Y** and a second molar equivalent of [**HY**] In the end, according to the proposed mechanism, the reduction of **H₂Y** affords a 2:1 mixture of [**HY**] and **H₄Y** (Eq. 5 in Fig. 14) As discussed above, this mechanism is mainly supported by the electrochemical and spectroscopic data revealing the accumulation of [**HY**] during the electrochemical reduction of **H₂Y**. It should however be mentioned that the presence of the colorless polyamine **H₄Y** (TD-DFT

calculated ($\lambda_{max\,theo}$ = 360 nm, 1200 $M^{-1}.cm^{-1}$ see Fig. 11) in the reaction media could so far not be demonstrated experimentally.

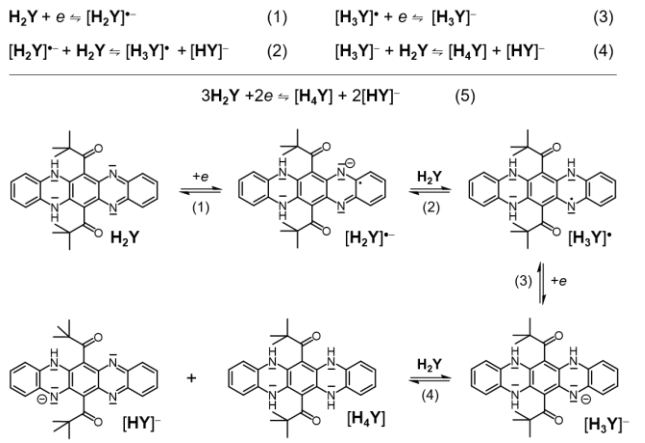

Fig. 14. Proposed mechanism following the reduction of **H_2Y**.

First oxidation of H_2Y. Similar SEC measurements were carried out in an attempt to identify the species generated upon the first oxidation of **H_2Y**. The absorption spectra collected when scanning the electrode potential from the OCP value (open circuit potential) up to E_3 = + 0.8 V are shown in Fig. 15a. What can be seen is *i)* the progressive disappearance of the initial signals attributed to **H_2Y** in favor of new signal featuring a maximum absorption at λ_{max} = 598 nm and *ii*) the existence of two well defined isosbestic points at λ = 449 and 552 nm. The reversibility of the chemical transformation coupled to the one-electron oxidation of **H_2Y** was moreover established from the data collected in Fig. 15b, showing that the spectrum of **H_2Y** can be fully recovered upon scanning back the electrode potential down to E_4 = −0.8 V.

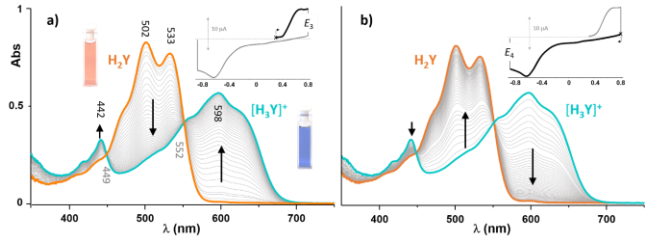

Fig. 15. UV-Vis spectra recorded over time for a solution of **H_2Y** (0.1 M $TBAPF_6$ in DCE) placed in a thin-layer spectroelectrochemical cell (0.5 mm, Pt grid) when the potential of the platinum grid was swept linearly a) from 0.4 V (OCP) to E_3 = +0.8 V at 20 $mV.s^{-1}$, followed by 5 minutes of potentiostatic electrolysis at +0.8 V) and b) from +0.8 V back to E_4 = −0.8 V at 20 $mV.s^{-1}$, followed by 5 minutes of potentiostatic electrolysis at −0.8 V.

First insights into the structure of the species produced at E_3 = +0.8 V came from EPR measurements revealing the diamagnetic character of the electrolysis product and from protonation studies showing that similar UV-Vis absorption spectra can be recorded after exhaustive oxidation at +0.8 V and after addition of excess TFA (see Fig. 7), the main characteristics being a broad absorption band centered at λ_{max} = 598 nm with shoulders at λ_{max} = 570 and 640 nm. Coulometry measurements also revealed that a full conversion of **H_2Y** requires abstraction of one electron per molecule. These results thus led us to propose the mechanism shown in Fig. 16 (Eq. 6 to 9) wherein the transient cation radical $[\mathbf{H_2Y}]^{+\bullet}$ is converted into the protonated species **$[H_3Y]^+$** by abstraction of H• from a solvent molecule. The abstraction of hydrogen from organic π-radicals is a quite rare reaction which has nevertheless already been observed with various heteroaromatic cation radicals based on porphyrin-, acridine- or diazodiphenylmethane- derivatives [67–72]. A problem common to all these studies is the difficulty of identifying the source of hydrogen which can potentially be attributed to solvent molecules such as acetonitrile, DMF or dichloromethane or even to the organic salts required for electrochemical measurements (in our case the tetra-*n*-butylammonium hexafluorophosphate). In line with these findings, the first step of the proposed mechanism is thus the one electron oxidation of **H_2Y** yielding $[\mathbf{H_2Y}]^{+\bullet}$ (Eq. 6 in Fig. 16) which is readily involved in a H transfer reaction (Eq. 7 in Fig. 16) involving a solvent molecule **SH** acting as a donor to afford the protonated product **$[H_3Y]^+$** together with a reactive solvent-based radical which eventually dimerizes (Eq. 8 in Fig. 16).

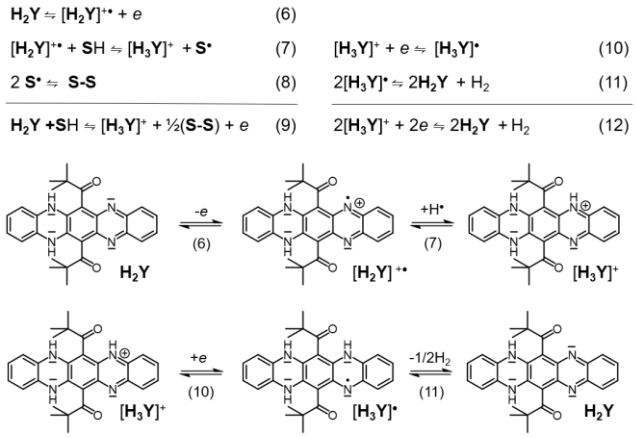

Fig. 16. Proposed mechanism following the oxidation of **H_2Y** at E_3.

The reversibility of the process, *i.e.,* the ability to recover the starting **H_2Y** species after back reduction of **$[H_3Y]^+$**, as revealed by the data shown in Fig. 15b**,** can be explained by considering that the one electron reduced species $[\mathbf{H_3Y}]^{\bullet}$ (Eq. 10 in Fig. 15) gets converted into **H_2Y** with hydrogen evolution (Eq. 10 to 12 in Fig. 16), as already hypothesized to occur with different porphyrin derivatives [73–75].

Second oxidation of H_2Y. Further investigations involved SEC measurements on the second oxidation wave, *i.e.,* upon scanning the electrode potential up to E_5 = +1.3 V. As expected, increasing the potential from E_{OCP} to +0.8 V (step 1 Fig. 17a) initially led to the accumulation of the protonated intermediate **$[H_3Y]^+$**, easily identifiable from the broad band developing at 598 nm. Scanning up to E_5 = +1.3 V (step 2 in Fig. 17a) then led to a progressive decrease in the intensity of that intermediate signal in favor of new bands developing at λ_{max} = 442, 519, 555 and 600 nm (Fig. 17a). Here again, these changes were found to be fully reversible in our experimental conditions, as proved by the data collected in Fig. 17b showing a complete recovery of the spectrum of **H_2Y** upon scanning back to E_6 = −1 V.

The spectrum collected after completion of the oxidation at E_5, exhibiting two weak signals above 500 nm; *i.e.,* at 555 and 600 nm, and a more intense one at λ_{max} = 442 nm, was in fact readily identified and attributed to the deprotonated analog **Y** (see Fig. 5). The series of electrochemical and chemical steps allowing to convert the protonated species **$[H_3Y]^+$** into **Y** are summarized in Fig. 18 (Eq. 13 to 17). The first step is the oxidation of the protonated species **$[H_3Y]^+$** yielding $[\mathbf{H_3Y}]^{2+\bullet}$ which readily evolves through loss of H^+ into $[\mathbf{H_2Y}]^{+\bullet}$. This intermediate is then expected to be spontaneously oxidized at E_5 to afford the doubly oxidized/protonated **$[H_2Y]^{2+}$** which releases both protons to yield the final reaction product **Y**. Once again, all our experimental findings and conclusion well match with the experimental and theoretical spectra of **$[H_3Y]^+$** and **Y** (see Fig. 10 and 11**)**. These attributions were further

supported by spectroelectrochemical analyses carried out on chemically prepared pure **Y** samples.

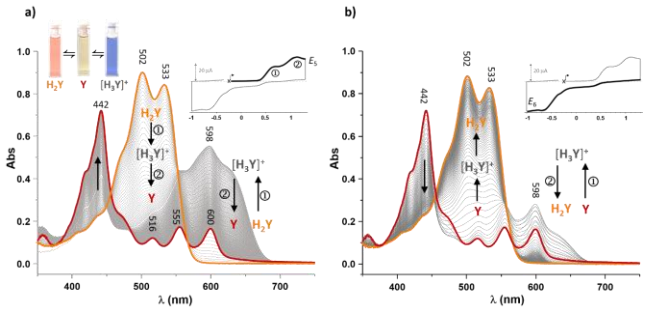

Fig. 17. UV-Vis spectra recorded over time for a solution of **H_2Y** (0.1 M $TBAPF_6$ in DCE) placed in a thin-layer spectroelectrochemical cell (0.5 mm, Pt grid) when the potential of the platinum grid was swept linearly a) from –0.4 V (OCP) to E_5 = +1.3 V at 20 mV.s^{-1}, followed by 5 minutes of potentiostatic electrolysis at E_5) and b) from +1.3 V back to E_6 = –1 V at 20 mV.s^{-1}, followed by 5 minutes of potentiostatic electrolysis at –1 V.

$[H_3Y]^+ \leftrightharpoons [H_3Y]^{2+\bullet} + e$ (13)

$[H_3Y]^{2+\bullet} \leftrightharpoons [H_2Y]^{+\bullet} + H^+$ (14)

$[H_2Y]^{+\bullet} \leftrightharpoons [H_2Y]^{2+} + e$ (15)

$[H_2Y]^{2+} \leftrightharpoons Y + 2H^+$ (16)

$[H_3Y]^+ \leftrightharpoons Y + 3H^+ + 2e$ (17)

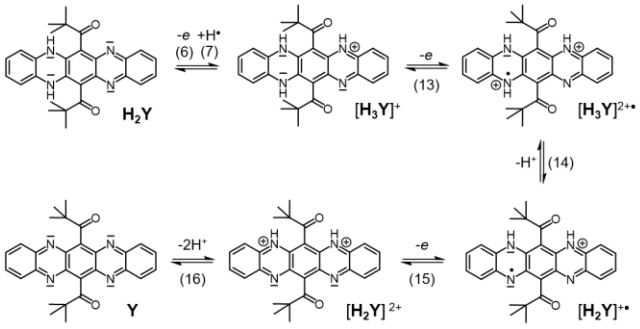

Fig. 18. Proposed mechanism following the oxidation of **H_2Y** at E_5.

Reduction of Y. The number of electrons involved in both reversible reduction CV waves observed in the accessible potential window, at $E_{1/2}$ = –0.610 V and $E_{1/2}$ = –1.165 V (Fig. 12a), was established from coulometric experiments coupled to UV-Vis measurements. Selected absorption spectra collected over time during the reduction of **Y** at E_{app} = −0.85 V are shown in Fig. 19a. These data bring to light that the spectrum of the electrogenerated species **[Y]**$^{-\bullet}$ displays intense signals at λ_{max} = 455, 769 and 856 nm as well as two less intense and broad ones in the NIR range, at λ_{max} = 1052 and 1226 nm. The clean formation of this stable radical anion was first revealed by the observation of a well-defined isosbestic point at λ = 448 nm. The stability of **[Y]**$^{-\bullet}$ was further demonstrated by electrochemical measurements carried out at static and rotating disk electrodes (RDE) after completion of the one-electron exhaustive reduction (Fig. 19c and Fig. 19d). The curves recorded at a RDE before and after electrolysis reveal that **[Y]**$^{-\bullet}$ is the unique product of the reaction and that it is stable in our conditions at the electrolysis time scale (≫1 hour). In agreement with the proposed structure, the X-band EPR spectra of **[Y]**$^{-\bullet}$ (Fig. 19b) recorded at room temperature is consistent with the presence of a single electron (g = 2.004) showing hyperfine interactions with 4 nitrogen atoms (a_N(G) = 1.15, 1.15, 1.63, 1.63) and 7 hydrogen atoms (a_H(G) = 0.57, 1.66, 1.66, 1.19, 1.19, 2.21, 2.214).

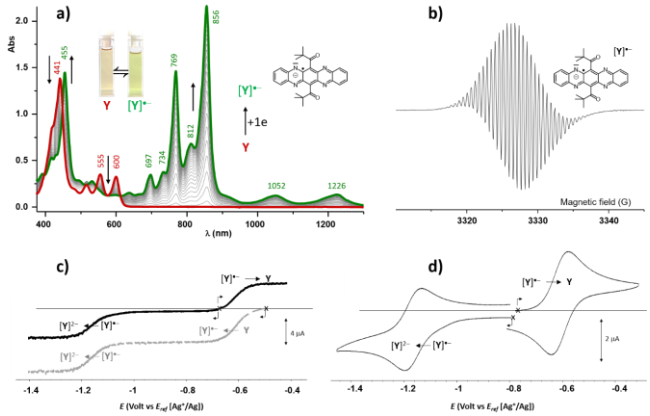

Fig. 19. a) UV-Vis spectra recorded over time during the exhaustive reduction (1 e/moles) of **Y** (0.5 mM in 10 mL of DCE + 0.1 M $TBAPF_6$) at E_7 = –0.85 V (Pt grid, l = 1mm). b) X-band EPR spectra recorded at RT after exhaustive reduction of **Y** at E_7 (1 e/moles). c) Voltamperometric curves recorded at a rotating disk electrode (ø = 3 mm, 0.01 V.s^{-1}, 500 rad.min^{-1}) before (grey line) and after (black line) exhaustive reduction of **Y** at E_7 (1 e/moles). d) Voltamperometric curves recorded at a static vitreous carbon working electrode (ø = 3 mm, 0. 1 V.s^{-1}) and after exhaustive reduction of **Y** at E_7 (1 e/moles).

In a second experiment, **Y** was submitted to a potentiostatic electrolysis at E_8 = –1.45 V in an attempt to generate and characterize the two-electron reduced species **[Y]**$^{2-}$. The absorption spectra collected over time during this experiment are collected in Fig. 20a. Formation of the intermediate anion radical **[Y]**$^{-\bullet}$ in the early stage of the electrolysis (step 1 in Fig. 20a, from 0 to 1 electron/moles exchanged) was revealed by the development of bands centered at λ_{max} = 455, 769, 856, 1052 and 1226 nm (# in Fig. 20). Further reduction of that species (1 to 2 e/moles exchanged) then led to the consumption of **[Y]**$^{-\bullet}$ in favor of a new set of intense signals centered at λ_{max} = 410, 593 and 635 nm (@ in Fig. 20a), which have previously been shown to be diagnostic features of **[HY]**$^{-}$ (see Fig. 6c and Eq. 13). This attribution was confirmed by RDE and CV measurements conducted after completion of the electrolysis (Fig. 20b and d) showing no trace of the expected dianion **[Y]**$^{2-}$ but only an irreversible wave at ~ –0.6 V attributed to the oxidation of the *in-situ* generated species **[HY]**$^{-}$ (see Fig. 13b and the associated discussion). The proposed mechanism to account for the formation of **[HY]**$^{-}$ by two-electron reduction of **Y** is shown in Fig. 22.

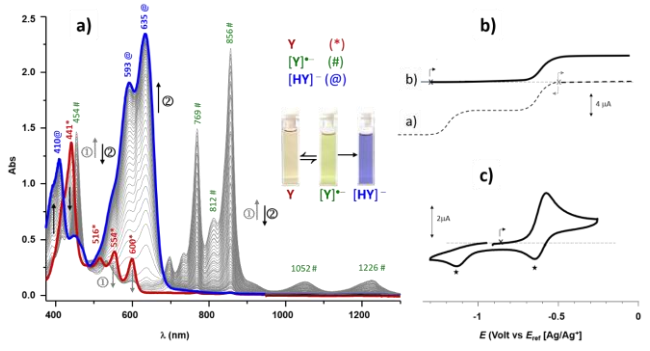

Fig. 20. a) UV-Vis spectra recorded over time during the exhaustive reduction (1 e/moles) of **Y** (0.5 mM in 10 mL of DCE + 0.1 M $TBAPF_6$) at E_8 = –1.45 V (Pt grid, l = 1mm). b) Voltamperometric curves recorded at a rotating disk electrode (ø = 3 mm, 0.01 V.s^{-1}, 500 rad.min^{-1}) before (dashed line) and after (black thick line) exhaustive reduction of **Y** at E_8 (1 e/moles). c) Voltamperometric curves recorded

at a static vitreous carbon working electrode (ø = 3 mm, 0. 1 V.s^{-1}) and after exhaustive reduction of **Y** at E_8 (1 e/moles).

The two first electrochemical steps are the successive one electron reduction of **Y** (Eq. 18 and 19 in Fig. 22) yielding the dianionic species [**Y**]$^{2-}$ which could not be observed in our experimental conditions as it spontaneously get protonated to afford [**HY**]$^-$ (Eq. 18 and 19 in Fig. 22). The source of proton in this reaction still remains unclear as all reactants have been carefully dried before use, but a plausible hypothesis is that it comes from protic impurities present in the electrolyte (solvent + 0.1 M $TBAPF_6$). A careful examination of the CV curve shown in Fig. 20c also reveals the presence of two weakly intense reduction waves at E_{pc} = –0.64 and –1.15 V (★ in Fig. 20c) on the backward scan which were attributed to the existence of chemical steps coupled to the one electron oxidation of [**HY**]$^-$. This assumption was confirmed upon carrying out an electrolysis of that compound at E_{app} = –0.25 V. The absorption spectra collected over time during this one electron oxidation as well as the electrochemical data collected after completion of the experiment are collected in Fig. 21.

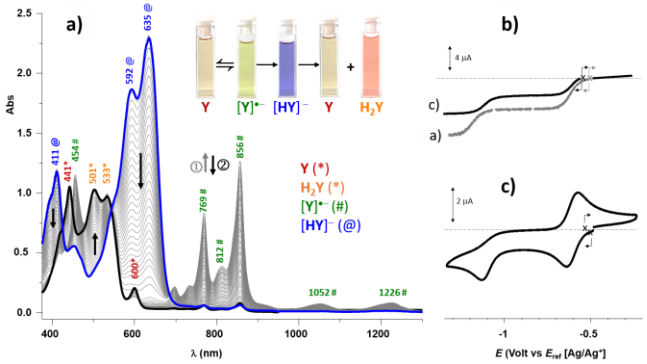

Fig. 21. a) UV-Vis spectra recorded over time during the exhaustive reduction (1 e/moles) of [**HY**]$^-$ (generated *in-situ* by reduction of **Y**, see Fig. 20) at E_9 = – 0.25 V (Pt grid, l = 1mm). b) Voltamperometric curves recorded at a rotating disk electrode (ø = 3 mm, 0.01 V.s^{-1}, 500 rad.min^{-1}) before (dashed line) and after (black thick line) exhaustive reduction of [**HY**]$^-$ at E_9 (1 e/moles). c) Voltamperometric curves recorded at a static vitreous carbon working electrode (ø = 3 mm, 0. 1 V.s^{-1}) after exhaustive reduction of **HY**$^-$ at E_9 (1 e/moles).

From a spectroscopic point of view, application of E_9 = –0.25V first led to a decrease in the intensity of the signals attributed to [**HY**]$^-$ and to the development of new bands at λ_{max} = 455, 769, 856, 1052 and 1226 nm (step 1 in Fig. 18) attributed to [**Y**]$^{\bullet-}$. This intermediate compound was then found to be transformed in the last stage of the experiment into a mixture of products featuring absorption maxima at 441, 501, 533 and 600 nm. These characteristic signals reaching maximum intensities after exchange of 1e/moles were readily attributed to an equimolar mixture of **Y** (441 and 600 nm) and **H_2Y** (501 and 533 nm). This attribution was then confirmed by electrochemical measurements (CV and LSV at RDE) with the observation of two consecutive reduction waves at $E_{1/2}$ = –0.605 V and Ep = –1.13 V, matching those obtained for **Y** (see Fig. 12a), and of an irreversible oxidation wave at E_p = 0.5 V (not shown on Fig. 12a, Figure S33) matching that observed for **H_2Y**. The stoichiometry of the reaction, initially assessed from the relative intensities of the bands attributed to **H_2Y** and **Y** in the spectra shown in Fig. 21a, was also confirmed upon comparing the intensities of the diffusion limited currents recorded at a RDE before (grey curve in Fig. 21b) and after (black curve in Fig. 21b) electrolysis. The loss of about half the intensity of the reduction waves centered on **Y** is indeed fully consistent with the conclusion that half the number of moles initially present in the cell could be recovered after one-electron oxidation of [**HY**]$^-$, the other half being converted into **H_2Y**. The PCET mechanism proposed to explain such behavior is detailed in Eq. 22-24, Fig. 22. It starts with the one electron oxidation of [**HY**]$^-$ yielding the neutral radical [**HY**]$^\bullet$ which reacts with the more basic species [**HY**]$^-$ through proton transfer to afford a mixture of **H_2Y** and **Y**$^{\bullet-}$. This latter anion radical is not stable at the applied potential E_9 and thus is oxidized into **Y**. This mechanism makes it possible to account for the stoichiometry of the transformation (Eq 24 in Fig. 20) and also, for the formation of **Y**$^{\bullet-}$ as an intermediate. The fact that **Y**$^{\bullet-}$ is not spontaneously oxidized at the electrode might be explained by the "slow" kinetics of Eq. 23 (Fig. 22).

$$\mathbf{Y} + e \leftrightharpoons [\mathbf{Y}]^{\bullet-} \quad (18)$$

$$[\mathbf{Y}]^{\bullet-} + e \leftrightharpoons [\mathbf{Y}]^{2-} \quad (19)$$

$$[\mathbf{Y}]^{2-} + H^+ \leftrightharpoons [\mathbf{HY}]^- \quad (20)$$

$$\mathbf{Y} + 2e + H^+ \leftrightharpoons [\mathbf{HY}]^- \quad (21)$$

$$[\mathbf{HY}]^- \leftrightharpoons [\mathbf{HY}]^\bullet + e \quad (22)$$

$$[\mathbf{HY}]^\bullet + [\mathbf{HY}]^- \leftrightharpoons \mathbf{Y}^{\bullet-} + \mathbf{H_2Y} \quad (23)$$

$$\mathbf{Y}^{\bullet-} \leftrightharpoons \mathbf{Y} + e \quad (22)$$

$$2[\mathbf{HY}]^- \leftrightharpoons \mathbf{H_2Y} + \mathbf{Y} + 2e \quad (24)$$

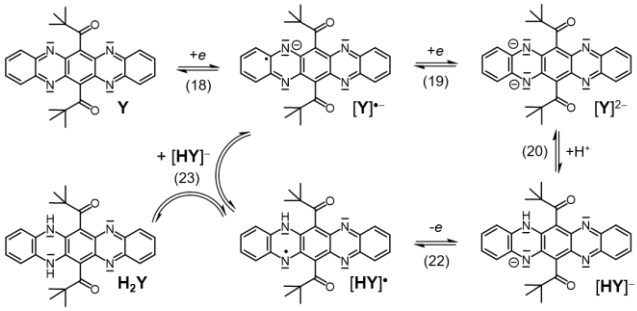

Fig. 22. Proposed mechanism following the reduction of Y at E_8 and the back oxidation of [**HY**]$^-$ at E_9.

4. Conclusion

We have reported herein the synthesis and characterization of a new tetraazapentacene derivative **Y**, and its corresponding dihydro form **H_2Y**, bearing electron-withdrawing pivaloyl moieties at positions 6 and 13. These bulky substituents led to the stabilization of the radical anion species **Y**$^{\bullet-}$ exhibiting fascinating NIR-absorption properties (from 700 to 1300 nm), which could be obtained either by chemical or electrochemical reduction of **Y** or by spontaneous O_2-mediated oxidation of **H_2Y** in basic conditions. We have then explored the electrochemical properties of both **H_2Y** and **Y**. These analyzes revealed the complex electrochemical/chemical pathways, involving H^+ or $H^\bullet$ transfer reactions, for switching from **H_2Y** to **Y**. All the proposed mechanisms and attributions are based on in-depth spectroscopic, electrochemical and spectroelectrochemical studies supported by vibrationally-resolved TD-DFT calculations. The reduction of **H_2Y** was found to afford the diamagnetic blue-colored anion [**HY**]$^-$ while the first oxidation of **H_2Y** led to a quantitative formation of the protonated species [H_3Y]$^+$ which could be further oxidized to yield the fully aromatic species **Y**. Our studies then brought to light the stability of the radical anion [**Y**]$^{\bullet-}$ featuring intense signals in the NIR region as well as a diagnostic EPR signal with hyperfine splitting. Further reduction of [**Y**]$^{\bullet-}$ then afforded an unstable dianion [**Y**]$^{2-}$ which was found to evolve through deprotonation into [**HY**]$^-$, a species that could be oxidized to produce a stoichiometric mixture of **Y** and **H_2Y**.

We have thus contributed to improving the knowledge on this class of molecules by highlighting the fascinating redox behavior of tetraazapentacene derivatives and by finely characterizing all the intermediate processes involved in the observed coupled processes. We hope that this detailed fundamental study will pave the way to applications of these molecules, in particular as redox–responsive dyes for electrochromism.

5. Acknowledgements

J.-F.L. wishes to thank the CNRS and the SATT sud-est for funding. C.B. wishes to thank the ENS de Lyon and the Région Auvergne-Rhône-Alpes for financial support. This work received support from the French Agence Nationale de la Recherche (ANR) under Contracts [ANR-20-CE29-0005] (BSE-Forces, Ph.D. grant of I.K.) and [ANR-21-CE07-0058-02] (Condor supporting the Marseille-Nantes collaboration). I.K. and D.J. are deeply indebted to the CCIPL/GliciD computational center for the always very generous allocation of computational time.

6. Conflicts of interests

There are no conflicts to declare

Appendix A. Supplementary data

Supplementary data associated with this article can be found, in the online version, at doi:10.1016/j.electacta…..

7. References

[1] E. Clar, Fr. John, Zur Kenntnis mehrkerniger aromatischer Kohlenwasserstoffe und ihrer Abkömmlinge, V. Mitteil.: Naphtho-anthracene, ihre Oxydationsprodukte und eine neue Klasse tiefgefärbter Kohlenwasserstoffe, Berichte Dtsch. Chem. Ges. B Ser. 62 (1929) 3021–3029. https://doi.org/10.1002/cber.19290621113.

[2] E. Clar, Fr. John, Über eine neue Klasse tiefgefärbter radikalischer Kohlenwasserstoffe und über das vermeintliche Pentacen von E. Philippi; gleichzeitig Erwiderung auf Bemerkungen von Roland Scholl und Oskar Boettger. (Zur Kenntnis mehrkerniger aromatischer Kohlenwasserstoffe und ihrer Abkömmlinge, VII. Mitteil.), Berichte Dtsch. Chem. Ges. B Ser. 63 (1930) 2967–2977. https://doi.org/10.1002/cber.19300631109.

[3] E. Clar, Fr. John, Zur Kenntnis mehrkerniger aromatischer Kohlenwasserstoffe und ihrer Abkömmlinge, VIII. Mitteil.: Über [Naphtho-2'3':1.2-anthracene],[2.3,6.7-Dibenzanthracen-9.10-diyle] und deren Oxydationsprodukte, Berichte Dtsch. Chem. Ges. B Ser. 64 (1931) 981–988. https://doi.org/10.1002/cber.19310640507.

[4] C. Tönshoff, H.F. Bettinger, Pushing the Limits of Acene Chemistry: The Recent Surge of Large Acenes, Chem. – Eur. J. 27 (2021) 3193–3212. https://doi.org/10.1002/chem.202003112.

[5] M. Kitamura, Y. Arakawa, Pentacene-based organic field-effect transistors, J. Phys. Condens. Matter. 20 (2008) 184011. https://doi.org/10.1088/0953-8984/20/18/184011.

[6] J.E. Anthony, J.S. Brooks, D.L. Eaton, S.R. Parkin, Functionalized Pentacene: Improved Electronic Properties from Control of Solid-State Order, J. Am. Chem. Soc. 123 (2001) 9482–9483. https://doi.org/10.1021/ja0162459.

[7] J.E. Anthony, Functionalized Acenes and Heteroacenes for Organic Electronics, Chem. Rev. 106 (2006) 5028–5048. https://doi.org/10.1021/cr050966z.

[8] Y. Yamashita, Organic semiconductors for organic field-effect transistors, Sci. Technol. Adv. Mater. 10 (2009) 024313. https://doi.org/10.1088/1468-6996/10/2/024313.

[9] U.H.F. Bunz, J.U. Engelhart, B.D. Lindner, M. Schaffroth, Large N-Heteroacenes: New Tricks for Very Old Dogs?, Angew. Chem. Int. Ed. 52 (2013) 3810–3821. https://doi.org/10.1002/anie.201209479.

[10] J.E. Anthony, The Larger Acenes: Versatile Organic Semiconductors, Angew. Chem. Int. Ed. 47 (2008) 452–483. https://doi.org/10.1002/anie.200604045.

[11] M.L. Tang, J.H. Oh, A.D. Reichardt, Z. Bao, Chlorination: A General Route toward Electron Transport in Organic Semiconductors, J. Am. Chem. Soc. 131 (2009) 3733–3740. https://doi.org/10.1021/ja809045s.

[12] C.R. Swartz, S.R. Parkin, J.E. Bullock, J.E. Anthony, A.C. Mayer, G.G. Malliaras, Synthesis and Characterization of Electron-Deficient Pentacenes, Org. Lett. 7 (2005) 3163–3166. https://doi.org/10.1021/ol050872b.

[13] Y. Sakamoto, T. Suzuki, M. Kobayashi, Y. Gao, Y. Fukai, Y. Inoue, F. Sato, S. Tokito, Perfluoropentacene: High-Performance p−n Junctions and Complementary Circuits with Pentacene, J. Am. Chem. Soc. 126 (2004) 8138–8140. https://doi.org/10.1021/ja0476258.

[14] M. Winkler, K.N. Houk, Nitrogen-Rich Oligoacenes: Candidates for n-Channel Organic Semiconductors, J. Am. Chem. Soc. 129 (2007) 1805–1815. https://doi.org/10.1021/ja067087u.

[15] T. Lelaidier, T. Leoni, P. Arumugam, A. Ranguis, C. Becker, O. Siri, Highly Ordered Molecular Films on Au(111): The N-Heteroacene Approach, Langmuir. 30 (2014) 5700–5704. https://doi.org/10.1021/la404214u.

[16] Lagrange, A.FR2864782, 2005.

[17] J. Manassen, S. Khalif, Organic Polymers. Correlation between Their Structure and Catalytic Activity in Heterogeneous Systems. II. Models for Dehydrogenation Catalysts, ACS Publ. (2002). https://doi.org/10.1021/ja00961a017.

[18] S.A. Jenekhe, Electroactive ladder polyquinoxalines. 1. Properties of the model compound 5,12-dihydro-5,7,12,14-tetraazapentacene and its complexes, Macromolecules. 24 (1991) 1–10. https://doi.org/10.1021/ma00001a001.

[19] H. Inoue, K. Noda, E. Imoto, The Electrical Conductivity of Heterocyclic Compounds. Fluoridine and Triphenodioxazine, Bull. Chem. Soc. Jpn. 37 (1964) 332–336. https://doi.org/10.1246/bcsj.37.332.

[20] Y. Ma, Y. Sun, Y. Liu, J. Gao, S. Chen, X. Sun, W. Qiu, G. Yu, G. Cui, W. Hu, D. Zhu, Organic thin film transistors based on stable amorphous ladder tetraazapentacenes semiconductors, J. Mater. Chem. 15 (2005) 4894–4898. https://doi.org/10.1039/B508594B.

[21] P.I. Lazarev, WO2007085810, 2007.

[22] M.B. Casu, P. Imperia, S. Schrader, B. Falk, Ultraviolet photoelectron spectroscopy of thin films of new materials for multilayer organic light emitting diodes, Surf. Sci. 482–485 (2001) 1205–1209. https://doi.org/10.1016/S0039-6028(01)00733-6.

[23] M.B. Casu, P. Imperia, S. Schrader, B. Falk, M. Jandke, P. Strohriegl, Ultraviolet photoelectron spectroscopy on new heterocyclic materials for multilayer organic light emitting diodes, Synth. Met. 124 (2001) 79–81. https://doi.org/10.1016/S0379-6779(01)00427-1.

[24] P.I. Lazarev, E.N. Sidorenko, A. Nokel, WO2007020442, 2007.

[25] M. Antinucci, B. Chevalier, A. Ferriolo, Development and characterisation of electrochromic devices on polymeric substrates, Sol. Energy Mater. Sol. Cells. 39 (1995) 271–287. https://doi.org/10.1016/0927-0248(95)00064-X.

[26] I. Johannsen, M. Jorgensen, WO9429314, 1994.

[27] S. Miao, A.L. Appleton, N. Berger, S. Barlow, S.R. Marder, K.I. Hardcastle, U.H.F. Bunz, 6,13-Diethynyl-5,7,12,14-tetraazapentacene, Chem. - Eur. J. 15 (2009) 4990–4993. https://doi.org/10.1002/chem.200900324.

[28] C. Amatore, G. Capobianco, G. Farnia, G. Sandona, J.M. Saveant, M.G. Severin, E. Vianello, Kinetics and mechanism of self-protonation reactions in organic electrochemical processes, J. Am. Chem. Soc. 107 (1985) 1815–1824. https://doi.org/10.1021/ja00293a003.

[29] J.M. Mayer, PROTON-COUPLED ELECTRON TRANSFER: A Reaction Chemist's View, Annu. Rev. Phys. Chem. 55 (2004) 363–390. https://doi.org/10.1146/annurev.physchem.55.091602.094446.

[30] C. Costentin, Electrochemical Approach to the Mechanistic Study of Proton-Coupled Electron Transfer, Chem. Rev. 108 (2008) 2145–2179. https://doi.org/10.1021/cr068065t.

[31] J. Armand, L. Boulares, C. Bellec, J. Pinson, Chemical and electrochemical reduction of pyrazino[2,3-g]quinoxalines and of their benzo and dibenzo derivatives; the structure of fluorindine and the formation of tetraanion, (n.d.) 5.
[32] L. Sawtschenko, K. Jobst, A. Neudeck, L. Dunsch, Electrochemical and spectroelectrocemical studies of dihydro-tetra-azapentacene as a model of polyazaacene, Electrochimica Acta. 41 (1996) 123–131. https://doi.org/10.1016/0013-4686(95)00277-L.
[33] J.E. Anthony, D.L. Eaton, S.R. Parkin, A Road Map to Stable, Soluble, Easily Crystallized Pentacene Derivatives, Org. Lett. 4 (2002) 15–18. https://doi.org/10.1021/ol0167356.
[34] M. Frisch, G. Trucks, H. Schlegel, G. Scuseria, M. Robb, J. Cheeseman, J. Montgomery, T. Vreven, K. Kudin, J. Burant, J. Millam, S. Iyengar, J. Tomasi, V. Barone, B. Mennucci, M. Cossi, G. Scalmani, N. Rega, G. Petersson, H. Nakatsuji, M. Hada, M. Ehara, K. Toyota, R. Fukuda, J. Hasegawa, M. Ishida, T. Nakajima, Y. Honda, O. Kitao, H. Nakai, M. Klene, X. Li, J. Knox, H. Hratchian, J. Cross, V. Bakken, C. Adamo, J. Jaramillo, R. Gomperts, R. Stratmann, O. Yazyev, A. Austin, R. Cammi, C. Pomelli, J. Ochterski, P. Ayala, K. Morokuma, G. Voth, P. Salvador, J. Dannenberg, V. Zakrzewski, S. Dapprich, A. Daniels, M. Strain, O. Farkas, D. Malick, A. Rabuck, K. Raghavachari, J. Foresman, J. Ortiz, Q. Cui, A. Baboul, S. Clifford, J. Cioslowski, B. Stefanov, G. Liu, A. Liashenko, P. Piskorz, I. Komaromi, R. Martin, D. Fox, T. Keith, A. Laham, C. Peng, A. Nanayakkara, M. Challacombe, P. Gill, B. Johnson, W. Chen, M. Wong, C. Gonzalez, J. Pople, Gaussian 16, Revision C.01, (2016).
[35] Y. Zhao, D.G. Truhlar, The M06 suite of density functionals for main group thermochemistry, thermochemical kinetics, noncovalent interactions, excited states, and transition elements: two new functionals and systematic testing of four M06-class functionals and 12 other functionals, Theor. Chem. Acc. 120 (2008) 215–241. https://doi.org/10.1007/s00214-007-0310-x.
[36] R. Cammi, B. Mennucci, Linear response theory for the polarizable continuum model, J. Chem. Phys. 110 (1999) 9877–9886. https://doi.org/10.1063/1.478861.
[37] T. Le Bahers, C. Adamo, I. Ciofini, A Qualitative Index of Spatial Extent in Charge-Transfer Excitations, J. Chem. Theory Comput. 7 (2011) 2498–2506. https://doi.org/10.1021/ct200308m.
[38] Z. Chen, C.S. Wannere, C. Corminboeuf, R. Puchta, P. von R. Schleyer, Nucleus-Independent Chemical Shifts (NICS) as an Aromaticity Criterion, Chem. Rev. 105 (2005) 3842–3888. https://doi.org/10.1021/cr030088+.
[39] FCclasses – CNR-ICCOM, (n.d.). http://www.iccom.cnr.it/en/fcclasses/ (accessed November 9, 2022).
[40] F. Santoro, R. Improta, A. Lami, J. Bloino, V. Barone, Effective method to compute Franck-Condon integrals for optical spectra of large molecules in solution, J. Chem. Phys. 126 (2007) 084509. https://doi.org/10.1063/1.2437197.
[41] F. Santoro, D. Jacquemin, Going beyond the vertical approximation with time-dependent density functional theory, WIREs Comput. Mol. Sci. 6 (2016) 460–486. https://doi.org/10.1002/wcms.1260.
[42] J. Cerezo, F. Santoro, Revisiting Vertical Models To Simulate the Line Shape of Electronic Spectra Adopting Cartesian and Internal Coordinates, J. Chem. Theory Comput. 12 (2016) 4970–4985. https://doi.org/10.1021/acs.jctc.6b00442.
[43] Q. Peng, Y. Yi, Z. Shuai, J. Shao, Excited state radiationless decay process with Duschinsky rotation effect: Formalism and implementation, J. Chem. Phys. 126 (2007) 114302. https://doi.org/10.1063/1.2710274.
[44] A. Humeniuk, M. Bužančić, J. Hoche, J. Cerezo, R. Mitrić, F. Santoro, V. Bonačić-Koutecký, Predicting fluorescence quantum yields for molecules in solution: A critical assessment of the harmonic approximation and the choice of the lineshape function, J. Chem. Phys. 152 (2020) 054107. https://doi.org/10.1063/1.5143212.
[45] Q. Ou, Q. Peng, Z. Shuai, Toward Quantitative Prediction of Fluorescence Quantum Efficiency by Combining Direct Vibrational Conversion and Surface Crossing: BODIPYs as an Example, J. Phys. Chem. Lett. 11 (2020) 7790–7797. https://doi.org/10.1021/acs.jpclett.0c02054.
[46] P. Rybczyński, M.H.E. Bousquet, A. Kaczmarek-Kędziera, B. Jędrzejewska, D. Jacquemin, B. Ośmiałowski, Controlling the fluorescence quantum yields of benzothiazole-difluoroborates by optimal substitution, Chem. Sci. 13 (2022) 13347–13360. https://doi.org/10.1039/D2SC05044G.
[47] O.V. Dolomanov, L.J. Bourhis, R.J. Gildea, J. a. K. Howard, H. Puschmann, OLEX2: a complete structure solution, refinement and analysis program, J. Appl. Crystallogr. 42 (2009) 339–341. https://doi.org/10.1107/S0021889808042726.
[48] G.M. Sheldrick, SHELXT – Integrated space-group and crystal-structure determination, Acta Crystallogr. Sect. Found. Adv. 71 (2015) 3–8. https://doi.org/10.1107/S2053273314026370.
[49] G.M. Sheldrick, Crystal structure refinement with SHELXL, Acta Crystallogr. Sect. C Struct. Chem. 71 (2015) 3–8. https://doi.org/10.1107/S2053229614024218.
[50] J. Armand, L. Boulares, C. Bellec, J. Pinson, Chemical and electrochemical reduction of pyrazino[2,3-g]quinoxalines and of their benzo and dibenzo derivatives; the structure of fluorindine and the formation of tetraanion, Can. J. Chem. (2011). https://doi.org/10.1139/v87-271.
[51] C. Seillan, H. Brisset, O. Siri, Efficient Synthesis of Substituted Dihydrotetraazapentacenes, Org. Lett. 10 (2008) 4013–4016. https://doi.org/10.1021/ol801509v.
[52] Q. Tang, J. Liu, H.S. Chan, Q. Miao, Benzenoid and Quinonoid Nitrogen-Containing Heteropentacenes, Chem. – Eur. J. 15 (2009) 3965–3969. https://doi.org/10.1002/chem.200900160.
[53] James. Keeler, Peter. Wothers, Why chemical reactions happen, Oxford University Press, Oxford, 2009.
[54] J.A. Berson, Kinetics, Thermodynamics, and the Problem of Selectivity: The Maturation of an Idea, Angew. Chem. Int. Ed. 45 (2006) 4724–4729. https://doi.org/10.1002/anie.200600229.
[55] H. Mayr, M. Breugst, A.R. Ofial, Farewell to the HSAB Treatment of Ambident Reactivity, Angew. Chem. Int. Ed. 50 (2011) 6470–6505. https://doi.org/10.1002/anie.201007100.
[56] L. Ji, A. Friedrich, I. Krummenacher, A. Eichhorn, H. Braunschweig, M. Moos, S. Hahn, F.L. Geyer, O. Tverskoy, J. Han, C. Lambert, A. Dreuw, T.B. Marder, U.H.F. Bunz, Preparation, Properties, and Structures of the Radical Anions and Dianions of Azapentacenes, J. Am. Chem. Soc. 139 (2017) 15968–15976. https://doi.org/10.1021/jacs.7b09460.
[57] L. Ji, M. Haehnel, I. Krummenacher, P. Biegger, F.L. Geyer, O. Tverskoy, M. Schaffroth, J. Han, A. Dreuw, T.B. Marder, U.H.F. Bunz, The Radical Anion and Dianion of Tetraazapentacene, Angew. Chem. Int. Ed. 55 (2016) 10498–10501. https://doi.org/10.1002/anie.201603177.
[58] Y. Kumar, S. Kumar, K. Mandal, P. Mukhopadhyay, Isolation of Tetracyano-Naphthalenediimide and Its Stable Planar Radical Anion, Angew. Chem. 130 (2018) 16556–16560. https://doi.org/10.1002/ange.201807836.
[59] B. Tang, J. Zhao, J.-F. Xu, X. Zhang, Tuning the stability of organic radicals: from covalent approaches to non-covalent approaches, Chem. Sci. 11 (2020) 1192–1204. https://doi.org/10.1039/C9SC06143F.
[60] S.S. Batsanov, Van der Waals Radii of Elements, 37 (2001) 15.
[61] M.A. Spackman, D. Jayatilaka, Hirshfeld surface analysis, CrystEngComm. 11 (2009) 19–32. https://doi.org/10.1039/B818330A.

[62] K.E. Maly, Acenes vs N-Heteroacenes: The Effect of N-Substitution on the Structural Features of Crystals of Polycyclic Aromatic Hydrocarbons, Cryst. Growth Des. 11 (2011) 5628–5633. https://doi.org/10.1021/cg201182p.
[63] B. Schatschneider, J. Phelps, S. Jezowski, A new parameter for classification of polycyclic aromatic hydrocarbon crystalline motifs: a Hirshfeld surface investigation, CrystEngComm. 13 (2011) 7216. https://doi.org/10.1039/c1ce05560g.
[64] M.J. Turner, J.J. McKinnon, S.K. Wolff, D.J. Grimwood, P.R. Spackman, D. Jayatilaka, M.A. Spackman, CrystalExplorer17 (2017), (2017).
[65] T.-B. Ren, W. Xu, W. Zhang, X.-X. Zhang, Z.-Y. Wang, Z. Xiang, L. Yuan, X.-B. Zhang, A General Method To Increase Stokes Shift by Introducing Alternating Vibronic Structures, J. Am. Chem. Soc. 140 (2018) 7716–7722. https://doi.org/10.1021/jacs.8b04404.
[66] G. Garrido, E. Koort, C. Ràfols, E. Bosch, T. Rodima, I. Leito, M. Rosés, Acid−Base Equilibria in Nonpolar Media. Absolute p K_a Scale of Bases in Tetrahydrofuran, J. Org. Chem. 71 (2006) 9062–9067. https://doi.org/10.1021/jo061432g.
[67] K.L. Handoo, J.-P. Cheng, V.D. Parker, Hydrogen atom abstraction by radical cations. The reactions of 9-substituted acridine radical cations with cyclohexa-1,4-diene, J. Chem. Soc. Perkin Trans. 2. (2001) 1476–1480. https://doi.org/10.1039/B102285G.
[68] V.D. Parker, Radical Reactivity of Radical Ions in Solution. Radical-Radical and Radical-Substrate Coupling Mechanisms, Acta Chim. Scand. 52 (1998) 154–159. https://doi.org/10.3891/acta.chem.scand.52-0145.
[69] V.D. Parker, D. Bethell, A Kinetic Characterization of the Reactions of Anion Radicals of Diazodiphenylmethane in Acetonitrile, Acta Chem. Scand. 35 (1981) 72–74. https://doi.org/10.3891/acta.chem.scand.35b-0072.
[70] V.D. Parker, C. Jin-Pei, K.L. Handoo, Transformation of Nitrogen-Containning Aromatic Radical Cations into Protonated Substrates, Acta Chim. Scand. 47 (1993) 626–628. https://doi.org/10.3891/acta.chem.scand.47-0626.
[71] C. Inisan, J.-Y. Saillard, R. Guilard, A. Tabard, Y.L. Mest, Electrooxidation of porphyrin free bases: fate of the π-cation radical, New J. Chem. 22 (1998) 823–830. https://doi.org/10.1039/A803974G.
[72] D.E. Bartak, W.C. Danen, M.D. Hawley, Coupling of nitrophenyl radicals and anions to form anion radicals, J. Org. Chem. 35 (1970) 1206–1208. https://doi.org/10.1021/jo00829a087.
[73] Y. Fang, P. Bhyrappa, Z. Ou, K.M. Kadish, Planar and Nonplanar Free-Base Tetraarylporphyrins: β-Pyrrole Substituents and Geometric Effects on Electrochemistry, Spectroelectrochemistry, and Protonation/Deprotonation Reactions in Nonaqueous Media, Chem. – Eur. J. 20 (2014) 524–532. https://doi.org/10.1002/chem.201303141.
[74] J. Shen, J. Shao, Z. Ou, W. E, B. Koszarna, D.T. Gryko, K.M. Kadish, Electrochemistry and Spectroelectrochemistry of meso-Substituted Free-Base Corroles in Nonaqueous Media: Reactions of (Cor)H3, [(Cor)H4]+, and [(Cor)H2]-, Inorg. Chem. 45 (2006) 2251–2265. https://doi.org/10.1021/ic051729h.
[75] S. Al Shehimy, D. Frath, E. Dumont, F. Chevallier, C. Bucher, Synthesis and Electrochemistry of Free-Base Porphyrins Bearing Trifluoromethyl meso-Substituents, ChemElectroChem. 9 (2022) e202101604. https://doi.org/10.1002/celc.202101604.